



## Dynamic immunoediting by macrophages in homologous recombination deficiency-stratified pancreatic ductal adenocarcinoma

Wei-Feng Hong<sup>a,b,c,d,1</sup>, Feng Zhang<sup>a,1</sup>, Nan Wang<sup>e,1</sup>, Jun-Ming Bi<sup>f</sup>, Ding-Wen Zhang<sup>a</sup>, Lu-Sheng Wei<sup>a</sup>, Zhen-Tao Song<sup>g</sup>, Gordon B. Mills<sup>h</sup>, Min-Min Chen<sup>i</sup>, Xue-Xin Li<sup>j,\*</sup>, Shi-Suo Du<sup>k,\*</sup>, Min Yu<sup>a,\*</sup>

<sup>a</sup> Department of Pancreas Center, Guangdong Provincial People's Hospital (Guangdong Academy of Medical Sciences), Southern Medical University, Guangzhou, Guangdong, China

<sup>b</sup> Department of Radiation Oncology, Zhejiang Cancer Hospital, Hangzhou 310005, China

<sup>c</sup> Hangzhou Institute of Medicine (HIM), Chinese Academy of Sciences, Hangzhou 310005, China

<sup>d</sup> Zhejiang Key Laboratory of Radiation Oncology, Hangzhou 310005, China

<sup>e</sup> Cosmos Wisdom Biotech, co. ltd, Building 10, No. 617 Jiner Road, Hangzhou, Zhejiang, China

<sup>f</sup> Department of Urology, Guangdong Provincial People's Hospital (Guangdong Academy of Medical Sciences), Southern Medical University, Guangzhou, Guangdong, China

<sup>g</sup> Mills Institute for Personalized Cancer Care, Fynn Biotechnologies Ltd. Jinan, Shandong, China

<sup>h</sup> Division of Oncological Sciences, Knight Cancer Institute, Oregon Health & Science University, Portland, USA

<sup>i</sup> Shenzhen Bay Laboratory, Shenzhen, Guangdong, China

<sup>j</sup> Department of Physiology and Pharmacology, Karolinska Institutet, Solna 17165, Sweden

<sup>k</sup> Department of Radiation Oncology, Cancer Center, Zhongshan Hospital, Fudan University, Shanghai, China

### ARTICLE INFO

#### Keywords:

Pancreatic ductal adenocarcinoma  
Homologous recombination deficiency  
Macrophage  
Spatial phenotypic-transcriptomic profiling  
Targeted therapy

### ABSTRACT

Pancreatic ductal adenocarcinoma (PDAC) is a lethal disease, notably resistant to existing therapies. Current research indicates that PDAC patients deficient in homologous recombination (HR) benefit from platinum-based treatments and poly-ADP-ribose polymerase inhibitors (PARPi). However, the effectiveness of PARPi in HR-deficient (HRD) PDAC is suboptimal, and significant challenges remain in fully understanding the distinct characteristics and implications of HRD-associated PDAC. We analyzed 16 PDAC patient-derived tissues, categorized by their homologous recombination deficiency (HRD) scores, and performed high-plex immunofluorescence analysis to define 20 cell phenotypes, thereby generating an in-situ PDAC tumor-immune landscape. Spatial phenotypic-transcriptomic profiling guided by regions-of-interest (ROIs) identified a crucial regulatory mechanism through localized tumor-adjacent macrophages, potentially in an HRD-dependent manner. Cellular neighborhood (CN) analysis further demonstrated the existence of macrophage-associated high-ordered cellular functional units in spatial contexts. Using our multi-omics spatial profiling strategy, we uncovered a dynamic macrophage-mediated regulatory axis linking HRD status with SIGLEC10 and CD52. These findings demonstrate the potential of targeting CD52 in combination with PARPi as a therapeutic intervention for PDAC.

### Statement of Significance

We characterized the spatial organization of the TME in PDAC by leveraging HRD levels as a key determinant, unveiling the intricate TME characteristics orchestrated by the dynamic pattern of macrophages. We discovered the therapeutic potential of SIGLEC10-CD52 axis mediated via macrophages, suggesting that CD52 may become a novel target for combinational therapy.

### Introduction

Pancreatic ductal adenocarcinoma (PDAC) is a deadly disease, recognized as one of the top causes of cancer-related mortality in many Western countries, with a 5-year survival rate seldom exceeding 12% (Huang et al., 2021; Siegel et al., 2023). Despite advancements in

\* Corresponding authors.

E-mail addresses: [xuexin.li@ki.se](mailto:xuexin.li@ki.se) (X.-X. Li), [du.shisuo@zs-hospital.sh.cn](mailto:du.shisuo@zs-hospital.sh.cn) (S.-S. Du), [yumin@gdph.org.cn](mailto:yumin@gdph.org.cn) (M. Yu).

<sup>1</sup> Weifeng Hong, Feng Zhang and Nan Wang contributed equally to this work.

targeted and immunotherapies for other aggressive cancers, PDAC treatment is predominantly dependent on chemotherapy (Huang et al., 2021). Approximately 77 % of PDAC patients have intrinsic resistance, and 23 % develop resistance after an initial partial response (Springfield et al., 2019; Lin et al., 2024). Currently, poly (ADP-ribose) polymerase inhibitors (PARPi) as being an effective therapy, are used specifically in a small subset of metastatic patients with germline BRCA1 or BRCA2 mutations (Golan et al., 2019). This approach, benefiting those with homologous recombination (HR) deficiencies, a key mechanism for repairing double-strand DNA breaks, marks a significant advancement by targeting the DNA damage response (DDR) pathway (Hong et al., 2024; Guantay et al., 2023). Moreover, PDAC patients with high HRD levels (often referred to as having "HRDness"), have shown superior responses to platinum-based treatments and PARPi, highlighting the importance of HRD status as a vital biomarker for patient stratification (Casolino et al., 2021; Aguirre et al., 2018). Nevertheless, the response rates in patients with dysfunctional BRCA1/2 or dMMR are relatively low (22.1 % and 18.2 % respectively) (Marabelle et al., 2020). While the therapeutic benefit of HRD has been clinically observed in PDAC, the efficacy of PARPi in HRD-associated PDAC remains dismal, with challenges persisting in fully understanding its unique characteristics.

Genetic aberrations in malignant cells often trigger reprogramming of the Tumor Microenvironment (TME) that plays a key role in driving tumorigenesis and therapeutic resistance (Li et al., 2017; Bianchi et al., 2023; de Visser and Joyce, 2023). The low tumor cellularity and desmoplastic nature of the PDAC microenvironment have complicated omic-driven profiling and limited the ability to translate studies of the TME into clinical utility (Cancer Genome Atlas Research Network, 2017; Capula et al., 2022). To fill this gap, single-cell RNA sequencing (scRNA-seq) has helped to deconvolute PDAC ecosystem both under the diseased settings and treatment-related conditions (Werba et al., 2023; Hwang et al., 2022; Elyada et al., 2019; Jia et al., 2022). Moreover, spatial transcriptomics (ST) has also helped in mapping gene expression patterns associated with disease phenotypes, enabling the discovery of distinct features and attributes of the TME in pancreatic cancer (Free-D-Pastor et al., 2021; Han et al., 2022; Li et al., 2022a). Alongside its direct impact on tumor cells, HRD has the potential to induce genomic instability, leading to the accumulation of mutations and heightened exposure of neoantigens by PDAC cells. This phenomenon enhances the opportunity for the immune system to engage an immune response (Chabanon et al., 2021; Mouw et al., 2017). A comprehensive investigation of the HRD-associated TME is crucial for uncovering the underlying mechanisms behind platinum/PARPi resistance and developing improved therapeutic strategies in PDAC.

In this study, we presented high-dimensional multi-omic spatial profiling of 12 PDAC tumors with different HRD status. We pre-screened 27 prospectively collected PDAC patients by measuring their HRD levels developed through a panel comprising HRD-related genes and other HRD genetic features, providing a quantitative score for each patient (here termed HRD-score) (Chen et al., 2023a; Zhu et al., 2022). We selected 12 patients to reflect three different HRD groups ( $\text{HRD}=0$ ,  $0 < \text{HRD} < 15$ ,  $\text{HRD} \geq 15$ ) and conducted 15-plex based cyclic immunofluorescence to characterize multiple immune cell types in situ. In parallel, we obtained deep spatial transcriptome data using digital spatial profiler (DSP) mapped to the same regions of interest (ROIs) and validated CD52 mediated pathway as a therapeutic potential in multiple model systems (Fig. 1A). Our findings not only offer a comprehensive spatial profiling of PDAC in relation to HRD levels but, more significantly, reveal a dynamic regulatory pattern of macrophages within the tumor-associated immune stroma that exhibits a strong correlation with HRD scores. This macrophage regulation may play a crucial role in shaping the composition and architecture of the PDAC TME. These findings hold the potential to facilitate the stratification of PDAC patients based on HRD levels and functional characteristics, leading to improved therapeutic outcomes.

## Results

### Defining PDAC patient's HRD level using sequencing-based HDR scoring approach

We classified patients into different groups based on their HRD levels, which were quantified using sequencing approaches. We prospectively enrolled 27 PDAC patients who underwent surgical resection and collected tumor, adjacent normal tissue and paired peripheral blood to provide germline background controls. Pathological evaluation was used to ensure at least 20 % neoplastic cellular content within each sample to meet criteria required for deep sequencing (Fig. 1B and Supplementary Fig. S1A). The genetic information generated a continuous integer for each patient namely HRDscore, a quantitative estimation of the tumor's HRD level (Fig. 1C, left). In our PDAC cohort, HRDscore above 15 was rare and out of 27 patients being analyzed, only 4 (14.8 %) were characterized by high HRD level with the highest HRDscore reaching 31. To avoid sampling bias that may affect subsequent analysis, we included 12 PDAC patients assigned into three predefined HRD groups (4 cases in each group) according to their HRDscore ( $\text{HRD} = 0$ ;  $\text{HRD} < 15$ ;  $\text{HRD} \geq 15$ ) (Fig. 1C, right). Additionally, we randomly sampled adjacent normal tissues from 4 patients in follow-up spatial profiling. Germline mutations of BRCA1 were captured in 5/12 patients (Supplementary Fig. S1B). Somatic, the frequently mutated gene KRAS was found in all 12 patients regardless of their HRD status (Fig. 1D), TP53 mutations were detected in most of PDAC patients with an elevated HRDscore (7 out of 8, two-sided Fisher exact test  $p=0.01$ ). Mutations of the cyclin dependent kinase inhibitor CDKN2A was present at a higher frequency in non-zero HDR patients (Fig. 1D). Of note, the TGF $\beta$  downstream target SMAD4 which has been shown to be altered in approximately 55 % of PDAC tumors in previous studies (Kadera et al., 2014) was only mutated in 17 % of patients in our study cohort (Fig. 1D) possibly due to the small sample enrolled.

### High-plexed in situ immunofluorescence delineates PDAC TME across HRD groups

In order to obtain a comprehensive phenotypic coverage of the PDAC tumor microenvironment (TME), we developed and optimized a 15-plex based antibody panel consisting of canonical markers targeting epithelial, fibroblast and innate and adaptive immune cell lineages, along with druggable checkpoint molecules PD-1/PD-L1 as well as Ki-67 as a key indicator of proliferating cells (Table S1). In sum, we defined 20 cell subtypes based on multiple marker combinations including T cell lineages (Fig. 2A and Supplementary Fig. S2). We selected 144 region-of-interests (ROIs) totaling 47,144 cells for downstream analysis and after removal of cells expressing more than three markers and data normalization, we generated a supervised cell lineage map using t-distributed stochastic neighbor embedding (t-SNE) (Fig. 2B and Supplementary Fig. S3-S4) with 15 distinct immune cell populations along with fibroblasts and 3 tumor cell populations (marked by Ki67 or PD-L1 positivity) (Supplementary Fig. S5). Consistent with previously reported work, the pancreatic ecosystem exhibited relatively low tumor purity across HRD groups (cancer tissues: 25.2–35.08 % and adjacent normal: 33.56 %) and high-level of infiltrated fibroblasts (cancer tissues: 45.22–55.25 % and adjacent normal: 23.91 %) (Fig. 2C left, Table S2) (Werba et al., 2023; Hwang et al., 2022). We found a biphasic pattern of proliferating tumor cells that increased dramatically from peritumor to  $\text{HRD}=0$  tumors, but descended with increasing HRD levels, a finding supported by previous work (Fig. 2C, right) (Liu et al., 2018). Of the immune cell populations, B cells showed a marked decreasing trend with adjacent normal having the highest proportion that declined in parallel with increasing HRDscore (2.67 %, 1.19 %, 0.89 % respectively Fig. 2C and Table S2). T cells populations were frequent in the pancreatic immune microenvironment highlighting the key role of T cells in PDAC pathophysiology (Fig. 2C) (Schalck et al., 2022). The PD-1/PD-L1

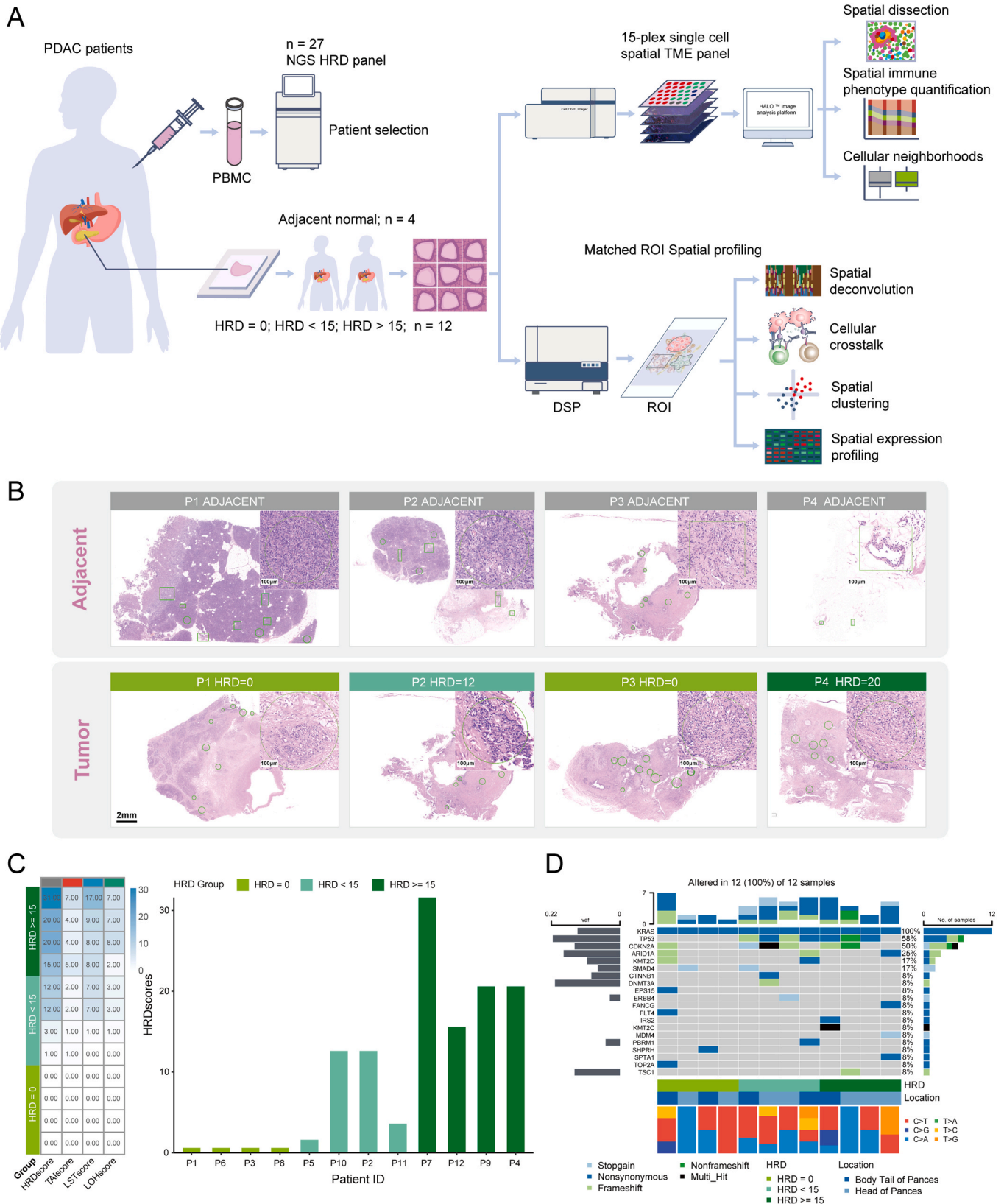


**Fig. 1. Study design of the multi-modal spatial profiling and genomic profiles of PDAC patients using targeted HRD-NGS panel.** A, Schematic illustration of the study. Patient's samples (tissues/paired bloods) were profiled through a pre-designed HRD panel. Selected 12 patients and 4 peritumor samples were subject to spatial profiling using 15-plex cyclic fluorescence and digital spatial profiler (DSP). B, Representative hematoxylin-eosin staining of PDAC tumor and normal tissue. C, Individual HRDscore parameters including TAIscore, LSTscore and LOHscore are shown and with blue colors (left) indicating the intensity with increasing HRDscore. HRDscore of patients assigned into corresponding groups are shown (right panel HRD=0, HRD<15, HRD≥15). D, Oncoplot showing the somatic mutations of 12 PDAC patients. Genetic alterations are color-annotated.

immune checkpoint levels were present at very low level independent of cell type (Supplementary Fig. S5). Macrophage states were presented at low levels in peritumor samples (adjacent) but increased in parallel with HDR levels (M1-like/M2-like: 7.17 %, 9.98 %, 13.14 % respectively Fig. 2C, Table S2). Subsequently, we categorized the region-of-interests (ROIs) into three distinct sub-locations, namely tumor/epithelium-enriched, peritumor immune-enriched, and fibroblast-enriched. This approach was undertaken to enhance the precision and accuracy of our assessment of the spatial organization within the tumor microenvironment. Pan-CK regions exhibited malignant epithelium with an increase in fibroblasts consistent with the high level of fibrosis in primary pancreatic cancer. While T cells were modestly increased in HRD 0 and HRD <15, they were markedly decreased in HRD >5 (Fig. 2D). In the immune-rich regions (CD45<sup>+</sup>), the HRD subtype exhibited a reduction in B cell populations and an augmentation of fibroblasts. Additionally, there was an increase in both M1-like and M2-like macrophage populations, with the most prominent increase observed in M1-like macrophages across the HRD subtypes (Fig. 2D, middle). We then profiled cell type co-presence across the HRD subtypes and found that the TME in high-HRD patients (HRD ≥15) showed macrophages were associated with multiple T-cell (cytotoxic T/helper T) subtypes and monocytes but dissociated with T regulatory cells, myeloid cells and fibroblasts confirming previous findings (Fig. 2E) (Jhunjhunwala et al., 2021). This was also consistent with the co-expression of macrophage markers with T cell subtype markers in immune-enriched ROIs (Supplementary Fig. S6B). Taken together, these data indicate that the immune-stromal microenvironment undergoes significant alterations during the transition from normal pancreatic tissue to PDAC. Moreover, the HRD status of tumor is closely linked to a distinct pattern of immune changes within this microenvironment. Remarkably, an HRD score of ≥15 exhibited a pronounced association with a substantial shift in macrophage abundance and differentiation.

#### Establishing an in-depth spatial transcriptional (ST) profile in PDAC across HRD groups

To elucidate mechanisms in the TME associated with different HRD levels, we performed spatial transcriptional profiling using Digital Spatial Profiler (DSP, nanoString, Seattle, whole transcriptome atlas, WTA) (Merritt et al., 2020) (Fig. 3A, Supplementary Fig. S7). To match the phenotype-transcriptome information described above, we matched ROIs between DSP profiling and high-plexed immunofluorescence. Although inter-patient heterogeneity existed, peritumor ROIs differed largely from neoplastic tissues indicating the robustness of the analysis (Fig. 3B). Tumor adjacent regions coalesce into a unified region, while tumor regions exhibit a singular axis and SMA<sup>+</sup> regions demonstrate two diverging branches that evolve from the adjacent regions (Supplementary Fig. S8A). In contrast there was no clear trajectory in the CD45 rich regions with adjacent cells being distributed along branches.

We then sought to apply SpatialDecon (a cell deconvolution algorithm) to resolve cellular contents across multiple HRD groups (Danaher et al., 2022). We used both a default input matrix (safeTME) and a PDAC-derived single-cell matrix (GSE155698 (Halbrook et al., 2022)) to obtain cell fractions (Fig. 3C, Supplementary Fig. S8B). The landscape-wise deconvolution revealed a significantly altered TME between adjacent regions and PDAC that featured a sharp reduction of pancreatic acinar cells and up-regulation of fibroblasts possibly myofibroblasts in SMA-enriched regions (Fig. 3C). An increase of antigen-presenting cancer-associated fibroblasts (apCAF), previously identified via scRNA-seq in PDAC (Hu et al., 2022), was found to a lesser extent within the immune regions predominantly in high HRD groups (HRD >15) (Fig. 3D). We also applied a series of computational methods (MCP-counter, consensusTME and EPIC) to prove existence of CAFs and confirmed an increase in CAFs in the tumor location in HRD-high patients (p < 0.05, Supplementary Fig. S9). The immune score was higher in tumor regions compared to adjacent normal but was not associated with

HRD status (Supplementary Fig. S9). However, while immune score was not markedly altered across the HRD subtypes, the immune composition was altered with a significant increase in macrophage populations (p < 0.05, Fig. 3D). M1/M2-like macrophage subtypes displayed a trend towards increases in tumors with elevated HRD levels, especially M2-like macrophages (Fig. 3E). T cells (mainly CD4<sup>+</sup> T cell, CD8 naïve T cell and CD8 memory T cell) exhibited a biphasic pattern which peaked in HRD=0 patients and dropped in higher HRD subtypes (Fig. 3D). To gain further insights into the regional changes of multiple cell types, we applied cell2location-WTA, a robust method for cellular phenotype estimation based on DSP data, to detect alterations in cell ratios within each HRD group (Li et al., 2022b). In peritumor normal samples PanCK regions had elevated levels of pro-inflammatory cells (CD4<sup>+</sup> T cell, CD8<sup>+</sup> T cell, NKs, macrophages and granulocytes) and anti-inflammatory Treg cells together with dynamic upregulation of myofibroblasts, and smooth muscle cells compared to malignant epithelium (p < 0.05 or trends), despite that many were present in low abundance (Fig. 3F and Supplementary Fig. S10). Of note, DC cells and B cells exhibited increasing trends during oncogenic transformation though both were present in trace amount. Biphasic changes of intra-tumoral apCAF, granulocytes, macrophages were also observed again highlighting their potential pro-inflammatory roles relating to altered HRD status (Supplementary Fig. S10). Similarly, fibroblasts-enriched regions were also signified by concomitant increase of myofibroblasts and smooth muscle cells and sharp decrease of pericytes indicating their opposing regulatory roles within the TME. Consistent with the aforementioned findings, our study confirms that macrophages undergo the most significant alterations within the immune-stromal region (p < 0.05 or trends), highlighting their pivotal role in governing the immune transition of HRD status (Supplementary Fig. S10).

#### Spatial gene expression patterns associated with HRDs

Given the importance of the HRD-related spatial changes in cell composition in PDAC, we investigated potential mechanisms that could explain the changes using DSP-WTA data. First, we looked at the shared and unique transcripts by comparing individual HDR groups with adjacent normal tissues in three locational compartments (PanCK<sup>+</sup> for tumor, CD45<sup>+</sup> for immune and SMA<sup>+</sup> for stroma). Within these, tumor epithelium displayed the highest number of differentially expressed genes (DEGs) (476/1833 with 476 shared genes in a total of 1833 differentially expressed genes across groups, FDR p < 0.05, log fold-change > 1) compared to the immune-stroma and fibroblast-enriched areas (65/604 and 215/762 respectively) (Fig. 4A, Supplementary Fig. S11). We then evaluated key pathways involved in those key spatial transcriptional programs using GO/KEGG gene enrichment analysis. In association with HRD levels, PanCK-rich region exhibited signatures of altered focal adhesion, extracellular remodeling, wound healing and ionic response. There was a significant association of antigen processing and presentation pathways observed across HRD subtypes within both the immune and stromal compartments (Fig. 4B-C, Supplementary Fig. S12). Subsequently, we extracted co-regulated gene sets specifically linked to individual spatial compartments. Our analysis revealed a set of genes that exhibited down-regulation between normal and PDAC states (adjacent versus HRD-nil groups), yet displayed upregulation with increasing HRD status. This gene set included MUC16, SPARC, AEBP1, RARRES1, and SUPT7L, all of which have been associated with tumorigenesis in the PanCK<sup>+</sup> region (Fig. 4D). In the CD45<sup>+</sup> regions, DUSP1, KDM5D, TSPY1, IFI6 and RNASE1 demonstrated a similar pattern (Fig. 4D). Another group of genes was maximally expressed in HRD-nil tumors including MMP1, TFF1, CEACAM5, B3GNT6 and MUCL3 in PanCK regions and C3, C7, MGP, JCHAIN and IGHA1 in SMA-rich regions (Fig. 4D, Supplementary Fig. S13). Together these spatial transcriptional programs depicted a dynamic PDAC TME that altered during oncogenic transformation and HRD state.

When utilizing cancer hallmark gene sets, we made a notable

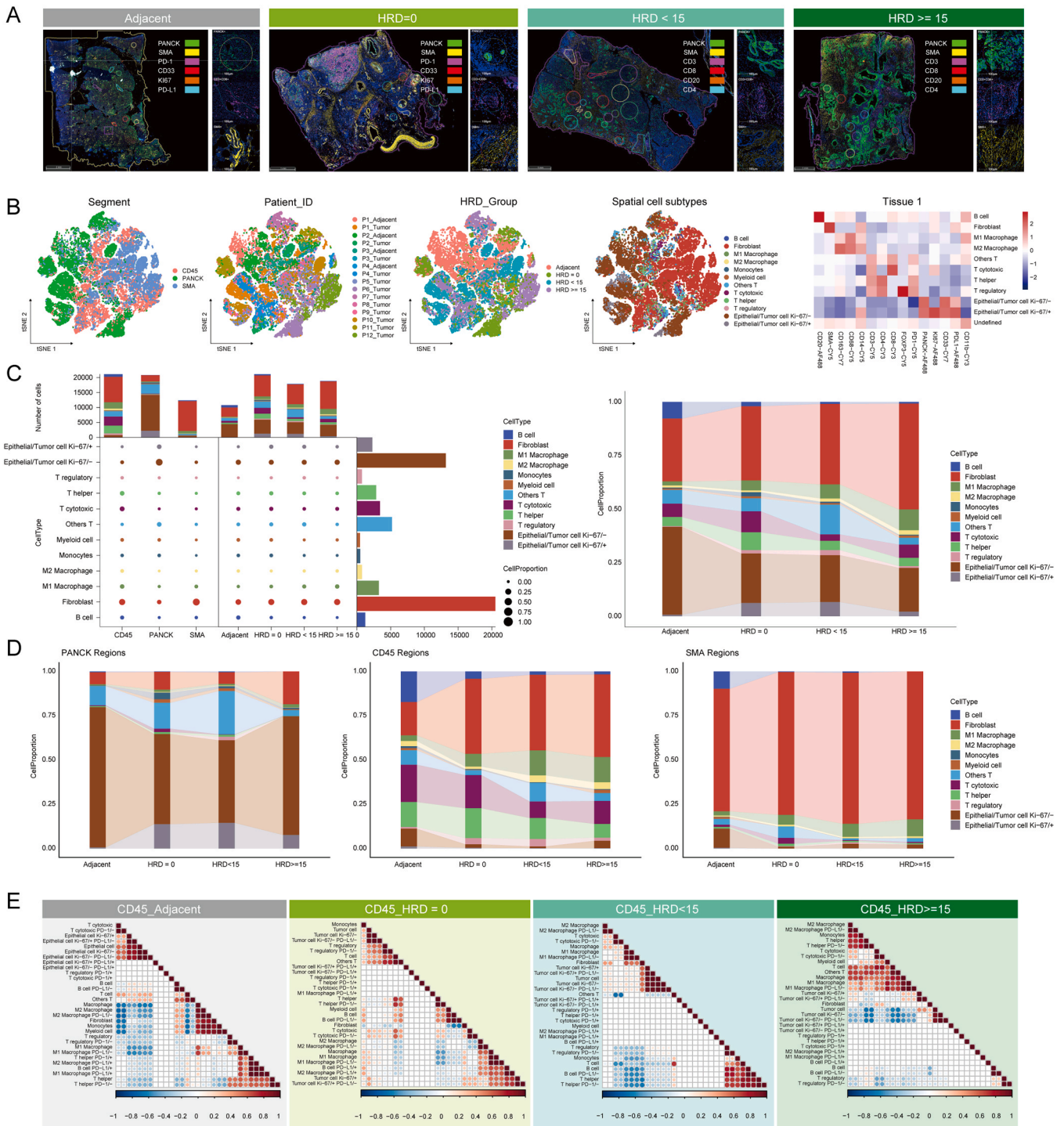


**Fig. 2. High-plex spatial single-cell immune profiling reveals phenotypic alterations associated with HRD status.** A, Representative fluorescence images of 15-plex panel in situ. Marker channels are shown separately. B, Unsupervised dimension reduction using t-SNE of all cells (47,144). Each cell in individual plots is assigned with their group annotations according to segment (location of ROI in tumor, immune-stroma or fibroblast-enriched regions respectively), patient ID, HRD status (grouped into adjacent, HRD=0, HRD<15, HRD≥15) and classification level 2 (marker-defined cell types excluding PD-L1 expression). Right figure: A patient with marker relative expression heatmap showing cell lineages based on classification level 2. C, (Left) Expression profiles (cell proportions) of individual cell types defined under classification level 2. Left panel shows cell profiles dissected into either three defined special locations (tumor, immune-stroma and fibroblast-enriched) or HRD status. Dots represent the averaged ratio of individual cell types across ROIs and for each ROI, cell types are summed to 100 %. (Right) Ribbon plot showing the cell type alterations between adjacent tissue and individual HRD groups. D, Ribbon plots showing the cell subtype alterations according to changing HRD status under spatial settings. Tumor (left), immune-stroma (middle) and fibroblasts (right) are shown separately. E, Inter-subtype correlations across ROIs within immune-enriched regions. Adjacent and HRD groups are shown in separate panels and Spearman correlation coefficients ( $R^2$ ) range from -1 (blue) to 1 (red).

observation that the transcriptional profiles associated with the homologous recombination (HR) pathway exhibited minimal correlation with the transition from adjacent normal tissue to tumor, as well as with HRD scores (Supplementary Fig. S14). This could potentially be due to the HR pathway transcriptomes being developed in different tumor lineages. The regulation of the extracellular matrix (ECM) exhibited substantial variations across the three spatial regions, characterized by dysregulated expression of LGALS4, FN1, COL5A1, COL1A2 and COL4A1 ( $p < 0.05$ ) (Supplementary Fig. S15). CAFs pathway-related genes exhibited inter-regional changes primarily at the tumor-fibroblast interface highlighted by altered COL6A3, LUM and FBLN1 ( $p < 0.05$ ) (Supplementary Fig. S15). We also identified a significantly upregulated antigen presentation signature at the tumor-surrounding immune regions that was associated with marked changes in class II major histocompatibility complex (MHC) molecules (HLA-DQB1, HLA-DQA1 and HLA-DMB,  $p < 0.05$ ) (Fig. 4E-F). There was also marked increase in tumor associated macrophages (TAMs) (CD68 and CD163,  $p < 0.05$ ) within this region (Fig. 4E-F). We also analyzed other MHC-class related genes and confirmed an increased expression of MHC II molecules present in HRD-high tumors ( $p < 0.05$ , Fig. 4F). Similarly, M2-like macrophage markers including CXCL10, CCL18 and MRC1 were increased in HRD-high tumors (Fig. 4E).

#### *Multicellular spatial interactions reveal macrophages-mediated spatial cellular neighborhood*

Considering the dynamic reprogramming of the TME, using ligand-receptor pairs from CellPhoneDB database, we constructed a spatial ligand-receptor map to extrapolate the spatial interaction for each HRD score (Garcia-Alonso et al., 2021). As HRD scores increased, tumor-immune interactions also increased whereas tumor-fibroblast interactions peaked in HRD-nil PDAC patients and gradually declined with increasing HRDscore (Supplementary Fig. S16A). These findings strongly indicate that the HRD status has the potential to modulate the immune-tumor interactions. We next looked at potential interaction pairs comparing adjacent regions to tumor regions and identified a trend towards CEACAM1/5/8 interacting with CD1D (DC markers), SELE (immune adhesion molecule) and CD209 (DC/M2 markers) while epithelial-derived fibroblast growth factor and receptor (FGF-FGFR) signals were completed lost ( $p < 0.05$ , Supplementary Fig. S17). Transition from adjacent to tumor was also associated with an increase in chemokine-driven interactions featured by CCL4L2-GPR101, CCL4L2-GPR152, CCL3-IDE, CCL3-CCR5, CCL3-CCR3, CCL3-CCR1 and CCL5-CCR1/3/4/5 ( $p < 0.05$ , Supplementary Fig. S17). The MHC II-class molecule CD74 interacting with MIF, COPA and APP was significantly increased ( $p < 0.05$ , Fig. 5B, Supplementary Fig. S15). Moreover, tumors with elevated HRDscore had elevated HLA interactions compared with HRD-nil patients, which was featured by MHC-I molecules HLA-E/C ( $p < 0.05$ , Supplementary Fig. S17). Interestingly, a series of macrophage-related signal cross-talk processes were associated with an increase in HRD score including APOB-TREM2 and CD28-CD80 (Supplementary Fig. S16B). Importantly, we noted two unique ligand-receptor pairs CD52-SIGLEC10 and CD44-SIGLEC15 present within the immune and epithelial regions respectively that were increased with transition from adjacent to tumor tissues and modestly increased with HRD status ( $p < 0.01$ , Fig. 5B, Supplementary Fig. S17). To further investigate, we extracted WTA data and conducted a comprehensive ROI-wise analysis of the correlation between the ligand-receptor pairs and individual spatial regions in different HRD groups. We discovered a positive correlation between both ligand-receptor pairs (CD52-SIGLEC10 and CD44-SIGLEC15) that correlate with elevated HRD scores ( $R^2 = 0.47$  and  $0.33$ , respectively) but not present in adjacent normal tissues ( $R^2 = -0.03$  and  $-0.34$ ) (Fig. 5A). Direct measuring of CD52-SIGLEC10 expression also demonstrated an up-regulation of this ligand-receptor pair at the tumor-surrounding areas (Fig. 5B-C).

We retrieved high-plexed immunofluorescence data and followed an existing approach to construct cellular neighborhoods (CNs) by first defining the ten nearest spatial neighbors for individual cells (Karimi et al., 2023). We then reclassified cells on the basis of their spatially annotated CNs across the entire tissue and from this, we repetitively captured 10 CNs within our PDAC tissue samples to define the TME, which we named: pan-immune (CN0), pan-immune tumor boundary (CN1), fibroblast-dominated (CN2), tumor-fibroblast interface (CN3), macrophage-involved tumor interface (CN4), pan-tumor-centric (CN5), fibroblast interacting immune (CN6), proliferating tumor (CN7), multi-marker cell hub (CN8), and other undefined cellular hub (CN9) (Fig. 5D). Due to the sample number limitations, we combined medium/high HRD patients into the same group and compared these with the HRD-nil group. We then screened individual CN frequencies with the relation to HRD phenotypes and associations with CN2, CN3 and CN4 and CD8 (Wilcoxon p-values range from 0.073 to 0.214 respectively) (Fig. 5E). CN8, characterized by undefined cells plus T helper, T reg and B cells tended to be associated with HRD-nil patients ( $p = 0.109$  as trend). CN2, a fibroblast-defined cluster, was enriched in PDAC TME in line with our data above (Werba et al., 2023). Besides, although present at low frequencies, the fibroblast-tumor interaction cluster (CN3) was shown to be significantly associated with tumor cells. Of further interest, though less frequent, the macrophage-tumor interaction cluster (CN4) was found to be spatially associated with tumors (CN5) and distinguished HRD-nil and non-zero HRD PDAC patients ( $p = 0.214$  as trend), again highlighting the importance of macrophage-mediated regulation in HRD high PDAC tumors (Fig. 6F, left). To verify the existence of the defined CNs, we then mapped ROIs accordingly the CN4/CN5 annotations in situ and profiled CD68/CD163 expression from the multiplex immunofluorescence. The resulting data confirmed elevated tumor sounding CD68<sup>+</sup> cells in non-zero HRD patients matching with our previous assumption (Wilcoxon rank sum test  $p = 0.024$ , Fig. 6F right). Lastly, we also explored the correlation of the spatial distribution of immune-enriched CD68<sup>+</sup> (M1-like) and CD163<sup>+</sup> (M2-like) macrophages, both of which were highly correlated with lymphatic invasion ( $p < 0.05$ ) (Supplementary Fig. S18).

Using paired transcriptomic and cell phenotypic data that allowed constructing a deconvolution method for pancreatic TME, we developed an R package (PDAC-Decon) that conducts deconvolution using our PDAC WTA spatial transcriptome data to identify across different tissue regions. Our internal validation yielded the best predicted average correlation of  $R^2 = 0.45$  with fibroblast having the highest predictive power ( $R^2 = 0.74$ ) (Supplementary Fig. S19, available on <https://github.com/HongWF413/PDAC-Decon>) for identification of different ROIs. This method will be optimized in future testing scenarios.

#### *Targeting CD52 confers therapeutic potentials in PDAC*

We sought to further test our hypothesis of this macrophage mediated tumor-immune response by conducting a series of experiments in model systems in vitro and in vivo. We began to induce THP-1 cells with PMA to generate macrophage-like cell phenotype. Then those cells were co-cultured with PANC-1 pancreatic cells prior to individual treatments (PARPi and anti-CD52) alone or in combinations and resulting cells were subject to flow cytometer analysis evaluating CD68 positivity. We noticed an induction of CD68<sup>+</sup> macrophage expression in response to single drug administration for either PARPi or anti-CD52 (Fig. 6A). Combined treatment of PARPi and anti-CD52 antibody further enhanced the CD68<sup>+</sup> macrophage expression, suggesting a probable mechanism that engages CD52 blockade to confer proliferation potentials of M1-like macrophages. We then went on to validate M1-like and M2-like markers in vitro and thus conducted ELISA based on PANC-1 co-cultured with induced THP-1 cells. We observed elevated IL6 and TNF (M1-like) levels when PARPi or anti-CD52 were treated together comparing with single agents alone (Fig. 6B-C) whereas M2-like markers IL10 and ARG1 were down-regulated (Fig. 6D-E). Next, immune competent C57BL/6 mice



**Fig. 3. Whole transcriptomic-based cell deconvolution uncovers major spatial cell alterations in the PDAC TME with varying HRD status.** A, Representative images from PDAC samples with fluorescent staining targeting epithelium (PanCK, green), immune (CD45, red) and fibroblasts ( $\alpha$ -SMA, yellow) regions. ROIs matching high-plex cyclic immunofluorescence are illustrated. B, Unsupervised dimension reduction using t-SNE of all ROIs. C, (Left) UMAP of PDAC single-cell RNAseq data and major cell types are annotated. (Right) cell deconvolution of spatial transcription data (SpatialDecon) using PDAC single-cell expression matrix. ROI allocations are shown according to designated spatial regions and HRD status. D, Spatial cell abundance changes associated with HRD (epithelial, immune and fibroblast regions are shown respectively). Asterisks indicate statistical significance. Right panel shows cell abundance changes according to HRD status and cell deconvolution is based on the default safeTME matrix. E, Expression of macrophages or M1/M2-like macrophages estimated via different deconvolution methods: SpatialDecon, xCell, EPIC and consensusTME. F, Cell2location-WTA mapping of cell abundance using PDAC single-cell data as the input matrix. ROI regions and HRD groups are annotated. Dots represent normalized absolute cell counts within ROIs and are averaged within groups. \*  $p < 0.05$ , \*\*  $p < 0.01$ , \*\*\*  $p < 0.001$ , \*\*\*\*  $p < 0.0001$ , ns: not significant.

were used wherein PAN02 cells were inoculated. Following PARPi and anti-CD52 single administration or combined, we quantified cells by flow cytometer. Similar to above findings, PARPi plus anti-CD52 was able to induce CD68<sup>+</sup> macrophages expression (Fig. 6F) suggesting an existing tendency of the positive regulation. Of further interests, the combined treatment significantly induced tumor regression (Fig. 6G).

We also attempted to explore the regulatory pathways mediated by macrophages after CD52 blockade. Using external scRNA-seq data, we discovered that the downstream effects might involve pathways such as “TGF- $\beta$  signaling” and “epithelial-mesenchymal transition (EMT)” (Supplementary Fig. S20A). Hence, we co-cultured PANC-1 and THP-1 cells and used western blotting to assess the impact of anti-CD52 blockade on TGF- $\beta$ 1 signaling and EMT under different concentration gradients. We showed that increasing concentrations of anti-CD52 significantly inhibited TGF- $\beta$ 1 signaling and EMT (Supplementary Fig. S20B-C). Additionally, we tested TGF- $\beta$ 1 stimulation in PANC-1 and BxPC-3 cells to establish an in vitro system of TGF- $\beta$ 1 signaling hyperactivation (Zhao et al., 2024). Western blotting analysis revealed that TGF- $\beta$ 1 stimulation significantly increased the protein levels of p-T $\beta$ R1, p-Smad2, and p-Smad3 in PANC-1 and BxPC-3 cells, while pre-treatment with anti-CD52 significantly reduced these protein levels (Supplementary Fig. S20D). Pre-treatment with anti-CD52 also significantly mitigated TGF- $\beta$ 1-induced EMT, as reflected in the inhibition of  $\alpha$ -SMA protein levels and the increase in E-cadherin protein levels in PANC-1 and BxPC-3 cells after TGF- $\beta$ 1 stimulation. This suggests that TGF- $\beta$ 1 signaling plays a crucial role in the impact of upon macrophage regulation in pancreatic cancer.

In summary, these findings further consolidate our assumption of macrophage-mediated tumor microenvironment regulation to facilitate the cytotoxic killing of tumor cells predisposed to significant DNA damage.

#### HRDscore mediated malignant program involves macrophage regulation

Since PDAC patients with different HRD status exhibit distinct immune pattern in the TME, we used WGCNA to identify transcriptional programs associated with HRD status and their relationship with various immune cells within the TME. First, we selected gene modules featuring key co-regulatory networks for each HRD group (most correlated gene sets/modules). We then correlated individual gene programs with HRD status and selected 8 top modules associated with each HRD group (top module-trait relationship  $R^2$  for tumor regions: Adjacent: 0.72, HRD=0: 0.45, HRD<15: 0.48 and HRD $\geq$ 15: 0.48 and top module-trait relationship  $R^2$  for fibroblast regions: Adjacent: 0.65, HRD=0: 0.44, HRD<15: 0.45 and HRD $\geq$ 15: 0.32) (Supplementary Fig. S21). Individual program genes were then filtered out from WTA and ssGSEA scores were calculated respectively. We used unsupervised clustered ROI-wise correlations between either individual ssGSEA scores or with a series of cell type abundance ratio calculated via the canonical deconvolution method (SpatialDecon). While immune cells co-clustered (Supplementary Fig. S22A), macrophage was associated with multiple cell types including fibroblasts ( $R^2=0.72$ ) and monocytes ( $R^2=0.55$ ) and to a lesser extent with endothelial cells ( $R^2=0.44$ ), myeloid DC ( $R^2=0.32$ ) and mast cells ( $R^2=0.36$ ). Besides, although most tumor/fibroblastic modules were grouped together, a malignant module from HRD $\geq$ 15

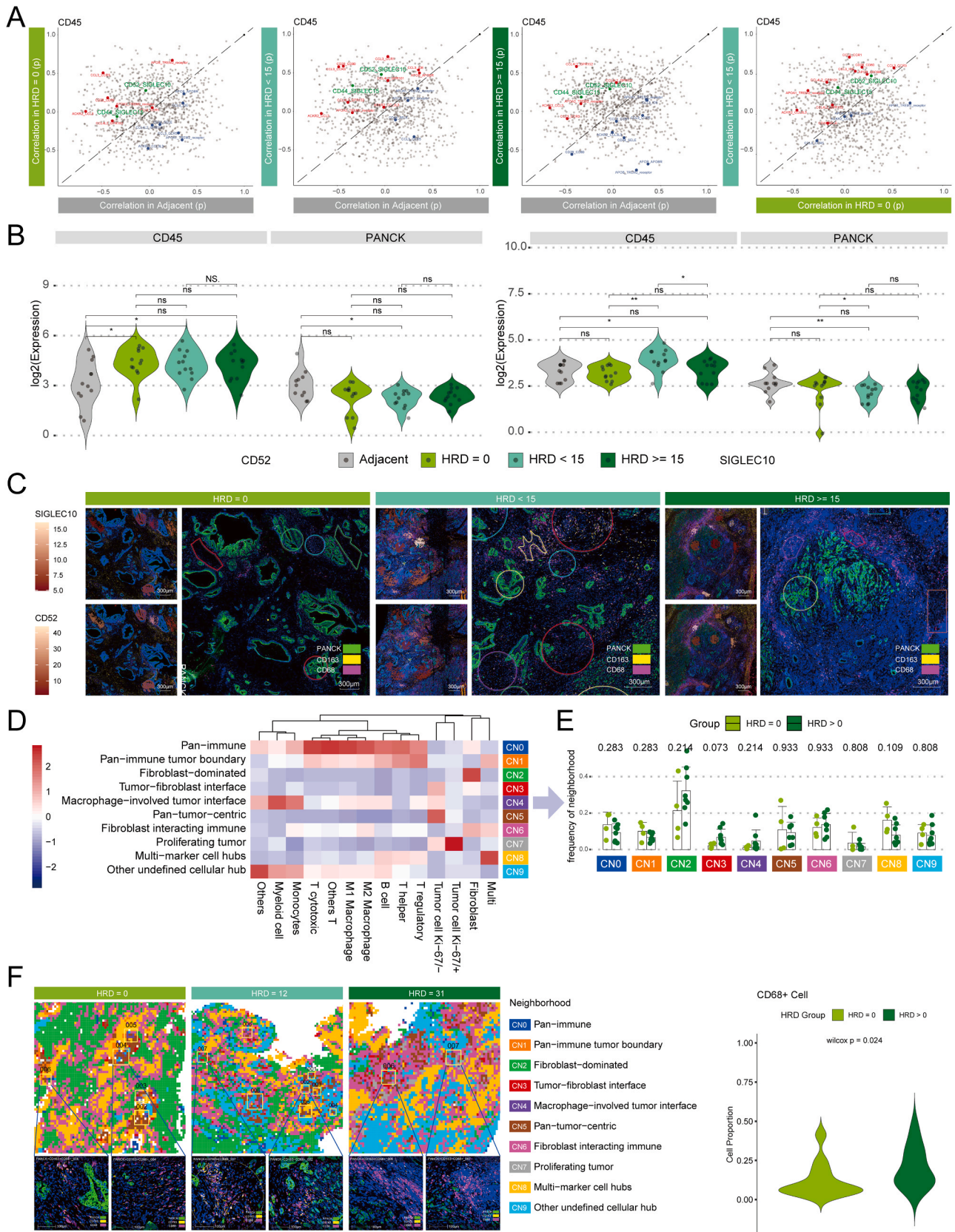
(module 4) had a distinct association with multiple cell types including endothelial cells, mast cells and fibroblasts (Supplementary Fig. S22A). Moreover, the highest association was found with macrophages ( $R^2=0.48$ ) again stressing a potentially important regulatory role of macrophages in HRD-high tumors (Supplementary Fig. S22A). Furthermore, we identified a tumorigenic expression module consisting of 284 genes and subsequently employed STRING and KEGG to construct functional sub-networks or interaction neighborhoods based on their functional annotations. These sub-networks revealed several crucial regulatory functions, such as RNA degradation, inflammation-associated NOD-like receptor signaling, autophagy, metabolic regulation, the Hippo signaling pathway, and proteoglycan regulation. Our analysis also revealed a significant association between the high-HRD malignant program and the PD-1/PD-L1 checkpoint highlighting a potential of synergistic effect of adding these ICI in high HRD patients (Supplementary Fig. S22B).

#### Discussion

Currently, genetic aberrations of BRCA1/2 and microsatellite instability (MSI) induced by impaired DNA repair pathway serve as patient stratification markers for platinum/PARPi-mediated therapies in PDAC (Golan et al., 2019; Lai et al., 2021). Although previous studies have described effects of BRCA1/2 mutation and mismatch repair deficiency (MMR) on remodeling of TME and infiltration of CD8<sup>+</sup> T cell (Samstein et al., 2021; Fraune et al., 2020), comprehensive spatially resolved molecular characterization has not been performed. A deeper understanding of the unique characteristics and implications of HR-deficient (HRD) PDAC is essential to better identify patients who may benefit from PARPi and platinum therapies and to understand the mechanisms underlying resistance to these treatments.

Here, we provided a high-dimensional spatial map of the pancreatic cancer TME based on HRD status using high-plexed immunofluorescence together with deep spatial transcriptome profiling (DSP). Our ROI-based analysis strategy on matched samples provides a benchmark towards future TME-oriented mechanistic exploration and in situ biomarker profiling. This spatial phenotypic-transcriptomic profiling increased the understanding of the complex PDAC tissue milieu and highlighted importance of the adding spatial-omic information to scRNA-seq analysis. Several TME features, including low PD-L1 expression, corroborate previous findings in the field (Nomi et al., 2007; Liang et al., 2018). Our findings revealed the presence of abundant cancer-associated fibroblasts (CAFs) in the TME of PDAC. Our data suggested that myofibroblast-derived CAFs (myCAFs) play a prominent role in fibroblast-enriched tissues surrounding the tumor. We observed a correlation between myCAFs and elevated HRD scores. This myCAFs population may contribute to tumor suppression and potentially interact with other cell lineages, such as macrophages, to create an inflamed TME in tumors with high HRD levels (Elyada et al., 2019; Ozdemir et al., 2014; Biffi et al., 2019; Han et al., 2021; Qin et al., 2024). These spatial findings corroborated previous scRNA-seq data, demonstrating the presence of various T cell subtypes (T helper, T regulatory, and T cytotoxic) and B memory cells in the TME of PDAC, regardless of HRD status (Werba et al., 2023; Schalck et al., 2022; Nguyen et al., 2020). Additionally, our spatial analysis revealed that CD4<sup>+</sup>/CD8<sup>+</sup>/NK T cells,





(caption on next page)

**Fig. 5. Spatial ligand-receptor interaction and cellular neighborhoods analysis implies potential macrophage-involved functional units linking with HRD status.** A, Spatial correlations of ligand-receptor pairs across HRD groups in immune compartments. Spearman rank correlation coefficients (ROI level) from individual HRD groups are used for inter HRD-group comparison. All ROIs from the CD45<sup>+</sup> regions are used and all HRD groups are compared to adjacent normal (annotated on vertical and horizontal axis). B, Violin plots showing CD52-SIGLEC10 ligand-receptor pairs in CD45<sup>+</sup> and PanCK<sup>+</sup> areas respectively. Normalized WTA data are used for comparison between different HRD groups. Statistical significance is shown. C, In-situ overlays of SIGLEC10 and CD52 gene expression from representative ROIs in different HRD groups. Scale bars show normalized expression counts from WTA. Matched fluorescence images showing PanCK, CD68 and CD163 protein expression are shown on the right of each panel. D, Heat map of cell types present within 10 CNs identified across all samples with their functional annotations (CN0-CN9). E, Comparison of CN distribution frequencies averaged across samples in HRD=0 (4 cases) and HRD>0 (8 cases including HRD<15 and HRD≥15). P-values are indicated on top. F, Schematic spatial cellular neighborhoods (CNs) in adjacent and different HRD tissue samples (HRD=0, 12 or 31). Individual CNs are color-annotated. CN4 (macrophage-involved tumor interface) is marked purple and CN5 (pan-tumor) is marked in brown. In situ fluorescence images of representative ROIs (CN4/CN5 containing) are shown below (PanCK<sup>+</sup>/CD68<sup>+</sup>/CD163<sup>+</sup>). Right panel: distribution of CD68<sup>+</sup> cells from ROIs obtained from high-plexed in situ immunofluorescence. ROIs were selected based on CN4 (macrophage involved) projected regions. \* p<0.05, \*\* p<0.01, ns: not significant.

granulocytes, and macrophages were infiltrating tumors while transitioning from nearby normal to malignant regions, but more critically, these cell types were notably more prevalent in tumors with high HRD levels. This was partly in line with previous studies using conventional IHC or computational tools (Ino et al., 2013; Carstens et al., 2017). CD8<sup>+</sup> T cell infiltration was previously found to be associated with down-regulated mismatch repair (MMR) proteins (MLH1, PMS2, MSH2 and MSH6) pointing at a DDR-mediated formation of a pro-inflammatory TME (Fraune et al., 2020). Tumor intrinsic mutational programs such as KRAS and TP53 are presumed contributors to the tumor-promoting TME in PDAC. However, in our cohort, KRAS mutations were unlikely to contribute to the effects of HRD-status since all patients carried mutant KRAS regardless of their HRD status (Hamarsheh et al., 2020; Chen et al., 2022). Dysfunctional TP53 present in 7 out of 8 in HRD-medium/high tumors in our cohort may contribute towards the TME remodeling associated with elevated HRD level. Additionally, our findings align with a general induction of reprogrammed tumor micro-environment (TME) around the tumor-stroma interface, demonstrating enhanced antigenic processing and presentation in tumors with elevated HRD (Ozdemir et al., 2014; Ubertini et al., 2015; Cooks et al., 2018). Our data suggested that the existence of HRD-induced genomic instability and dysregulated DNA repair pathways contributes towards spatially altered molecular pathways and cellular phenotypes.

Our identification of an increased in macrophages associated with elevated HRD levels was evident at both spatial phenotypic and spatial transcriptional levels. The spatial profiles revealed changes in both M1 and M2-like phenotypes. A M1-like phenotype may be functionally predominant in HRD-high tumors since pro-inflammatory IL18/CXCL10, T-cell mediating CD80/CD86 TNF-alpha exhibited a trend towards association with elevated HRD whereas a decrease was observed for the tumor inhibitory M2-like/TAM-like cytokine IL10 (Chavez-Galan et al., 2015; Mantovani et al., 2022; Reschke and Gajewski, 2022; Chen et al., 2023b). It is intriguing to hypothesize that the M1-like/M2-like macrophage changes contribute to the inflamed environment in HRD high tumors and potentially to the improved outcomes for these patients, a finding previously proven in mouse models (Zhang et al., 2021a). Our spatial transcriptional profiles uncovered evidences for antigen presentation via MHC II class molecules (a major anti-tumor mechanism of macrophage mediated activation) within the TME in association with elevated HRD levels supporting the contention that enhanced antigen presentation mediated via M1-like macrophages could contribute to the inflamed TME. In addition, MHC II-high TAM may play a role in antitumor immunity (Movahedi et al., 2010). Other M1/M2 related markers were less evident in high HRD patients (HRD≥15) potentially attributed to the mixed cell population within each ROI particularly in CD45-enriched regions (Wang et al., 2021a). Indeed, our spatial cell-cell interaction analysis suggested that macrophages demonstrated high degrees of spatial interaction with other immune cells. Nevertheless, M2-like macrophages may contribute to the outcomes of high HRD tumors as concomitant wound healing and ECM tissue remodeling phenomenon was observed in our gene enrichment analysis which can be associated with M2-like macrophage function (Zhang et al., 2021b; Herold et al., 2011). The wound healing function of

M2-like macrophages may contribute to eradication of unwanted cells post damaged tissue repair (Krzyszczuk et al., 2018). Our spatial transcriptomic data stemming from peritumor stroma, together with annotated biological functions supported an activated wound healing phenotype (M2a) since CD206 (MRC1), CD163 and MHC-II molecules were coordinately upregulated with elevated HRDscore (Ogle et al., 2016). In addition, there could be a mixed population of M2b macrophages (an immune-suppressive M2 subtype) present within TME since CD86, CD68 and MHC II were co-expressed in our spatial profiling data (Krzyszczuk et al., 2018; Hesketh et al., 2017). More importantly, our spatial cellular neighborhood (CN)-based analysis extended our ROI-based spatial discovery and demonstrated a macrophage-mediated (mostly M1-like) high-ordered spatial structure that is potentially functionally important in HRD-driven PDAC.

Through our investigation, we have observed an elevation in macrophage abundance associated with elevated HRD levels, as supported by both spatial phenotypic and spatial transcriptional analyses. This finding is particularly noteworthy considering the crucial functions fulfilled by macrophages in pancreatic cancer. It prompts further investigation into the mechanisms underlying the observed low response rate and drug resistance in HRD-associated PDAC cases, especially when PARPi are utilized. Nonetheless, additional experiments are required to provide insights into the underlying mechanisms driving these phenomena.

Based on our spatial ligand-receptor analysis, crosstalk between immune-stroma and malignant tissue was increased whereas tumor-fibroblast crosstalk was attenuated with elevated HRD levels. This suggests that HRD is associated with a dynamic interaction pattern. Our ligand-receptor spatial analysis suggested that some of these changes could be orchestrated by macrophages. For instance, co-regulation of interaction pairs such as immune-stroma APP-TREM2 and APOE-TREM2 is consistent with a macrophage-mediated modulation. TREM2 can promote oncogenic transformation and facilitate immune escape (Hamerman et al., 2006; Qiu et al., 2021; Hao et al., 2022). Blocking TREM2 signaling in macrophages has been shown to synergize with T cell-mediated anti-tumor immune response in tumors expressing PD-L1 (Hamerman et al., 2006; Deczkowska et al., 2020; Molgora et al., 2020). Additionally, TREM2-hi macrophages can lead to resistance to immune checkpoint therapy again highlighting an important role in regulation local immunogenicity (Xiong et al., 2020). Our focused analysis on macrophages as a strong indicator for lymphatic invasion and the presumable macrophage mediated CD52-SIGLEC10 communication in pancreatic cancer suffering excessive DNA damage may not only direct biomarker-oriented clinical intervention but may also elucidate additional therapeutic targets and this was strengthened by or in vitro and in vivo profiling (Werba et al., 2023; Wang et al., 2019; Liu et al., 2021; Bandala-Sanchez et al., 2013, 2018; Liu et al., 2023; Kung and Yu, 2023). Unleashing this checkpoint pathway in patients with an elevated HRD score may cooperate with platinum/PARPi administration together with anti-CD52 antibody to enhance local cytotoxicity and improve therapeutic responses of. Since strategies to target these glycans have already been explored in clinical settings, our data, for the first time, open up a new avenue of exploration in PDAC patients with high HRD

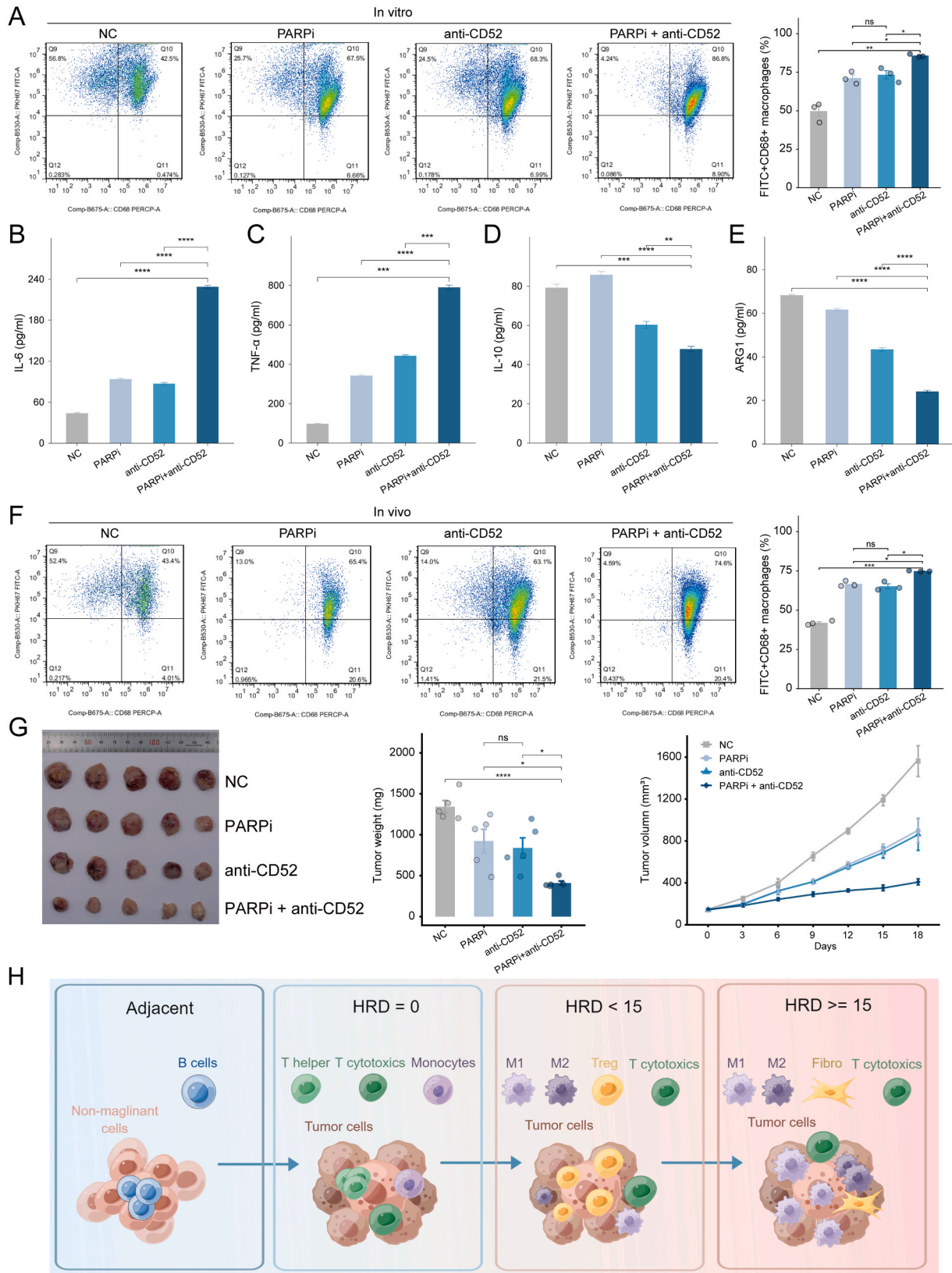


**Fig. 6. Anti-CD52 in conjunction with PARPi to suppress PDAC progression.** A, In vitro flow cytometry analysis of FITC<sup>+</sup>CD68<sup>+</sup> macrophage proportions across various groups. B-C, ELISA detection of IL-6 and TNF-α expression in PANC-1 and THP-1 co-cultures under diverse conditions. D-E, ELISA detection of IL-10 and ARG1 expression in PANC-1 and THP-1 co-cultures under varying conditions. F, In vivo flow cytometry analysis of FITC<sup>+</sup>CD68<sup>+</sup> macrophage proportions in tumor tissues under differing conditions. G, Comparative assessment of tumor size, weight, and volume among the NC group, PARPi group, anti-CD52 group, and combined group of mice. H, Illustrative diagram delineating the mechanism of the macrophage-mediated regulatory network in PDAC TME during oncogenesis and transformation of HRD status. \* p<0.05, \*\* p<0.01, \*\*\* p<0.001, ns: not significant.

based on their HRD status (Smith and Bertozzi, 2021). However, due to the limited sample size, further validations at spatial single-cell level in larger clinical cohorts and mechanistic elucidation are needed to facilitate translation into clinical application.

In conclusion, our study utilized highly resolved spatial transcriptomic-phenotypic profiles and conducted comprehensive bioinformatic analysis, revealing a potential macrophage-driven immune reprogramming within the PDAC TME (Fig. 6H). This immune modulation has the potential to establish a connection between aberrant DNA repair pathways in PDAC and the presence of an inflamed TME. Understanding this link is crucial for investigating the underlying factors contributing to the observed low response rate and drug resistance in HRD-associated PDAC cases. By expanding the sample size, this research could lead to the identification of biomarkers that are prognostic for lymphatic-mediated metastasis, enhancing the stratification of patients who are likely to benefit from platinum/PARP*i* treatments. Importantly, the SIGLEC10-CD52 checkpoints may emerge as novel, actionable therapeutic targets in PDAC patients with elevated HRD levels. The combination of CD52 blockade and PARP inhibitors could potentially become the new care for patients with HR-deficient pancreatic cancer.

## Methods

### *Clinical sample procurement*

This study was ethically approved by the Institutional Review Board of Guangdong Provincial People's Hospital (KY2023-161-01). We prospectively collected samples from 27 patients with pancreatic ductal adenocarcinoma (PDAC) who underwent routine surgical resection. All patients were treatment naïve prior to surgery. Pathological assessment of PDAC samples was confirmed by two senior pathologists independently. Samples containing tumor contents of more than 20% were considered as inclusion criteria. All paired tumor tissues, adjacent non-tumor pancreatic tissue, and peripheral blood were collected and subject to downstream analysis.

### *Tissue evaluation, processing and genomic DNA extraction*

Formalin-fixed paraffin-embedded (FFPE) tissue sections were evaluated for tumor cellular contents using hematoxylin and eosin (H&E) staining. Samples were deparaffinized with mineral oil and then incubated with lysis buffer and proteinase K at 56 °C overnight until the tissues were completely digested. The lysates were subsequently incubated at 80 °C for 4 hours to reverse crosslinking. Genomic DNA was isolated from tissue samples using the ReliaPrep™ FFPE gDNA Miniprep System (Promega) and quantified using the Qubit™ dsDNA HS Assay Kit (Thermo Fisher Scientific) following the manufacturer's instructions.

### *Library construction and tissue-based targeted capture using HRD sequencing panel*

DNA extracts (30–200 ng) were sheared to 250 bp fragments using an S220 focused-ultrasonicator (Covaris). Libraries were prepared using the KAPA Hyper Prep Kit (KAPA Biosystems) following the manufacturer's protocol. The concentration and size distribution of each library were determined using a Qubit 3.0 fluorometer (Thermo Fisher Scientific) and a LabChip GX Touch HT Analyzer (PerkinElmer) respectively. For targeted capture, indexed libraries were subjected to probe-based hybridization with a customized NGS panel targeting 139 HRD and key oncogenic driver genes, wherein the probe baits were designed as 5' biotinylated 120 bp DNA oligonucleotides individually. Repetitive elements were filtered out from intronic baits according to the annotation by UCSC Genome RepeatMasker (Karolchik et al., 2004). The xGen® Hybridization and Wash Kit were employed for hybridization enrichment. Briefly, 500 ng indexed DNA libraries were pooled to obtain a total amount of 2 µg of DNA. The pooled DNA samples were then mixed

with human cot DNA and xGen Universal Blockers-TS Mix and dried down in a SpeedVac system. The Hybridization Master Mix was added to the samples and incubated in a thermal cycler at 95°C for 10 mins, before being mixed and incubated with 4 µl of probes at 65°C overnight. The target regions were captured following the manufacturer's instructions. The concentration and fragment size distribution of the final library were determined using a Qubit 3.0 fluorometer (Thermo Fisher Scientific) and a LabChip GX Touch HT Analyzer (PerkinElmer) respectively.

### *DNA sequencing, data processing, and variant calling for tissue-based testing*

The captured libraries were processed with a NovaSeq 6000 NGS platform (Illumina) for paired-end sequencing (100 cycles) with at least a sequencing depth of 500X. Raw data of paired samples (an FFPE sample and its normal tissue control) were mapped to the reference human genome hg19 using the Burrows-Wheeler Aligner (v0.7.12) (Li and Durbin, 2009). PCR duplicate reads were removed and sequence metrics were collected using Picard (v1.130) and SAMtools (v1.1.19), respectively. Variant calling was performed only in the targeted regions. Somatic single nucleotide variants (SNVs) were detected using an in-house developed R package to execute a variant detection model based on binomial test. Local realignment was performed to detect indels. Variants were then filtered by their unique supporting read depth, strand bias, base quality as previously described (Su et al., 2017). All variants were then filtered using an automated false positive filtering pipeline to ensure sensitivity and specificity at an allele frequency (AF) of  $\geq 5\%$ . Single-nucleotide polymorphism (SNPs) and indels were annotated by ANNOVAR against the following databases: dbSNP (v138), 1000 Genome and ESP6500 (population frequency  $> 0.015$ ). Only missense, stopgain, frameshift and non-frameshift indel mutations were kept. Copy number variations (CNVs) and gene rearrangements were detected as described previously (Su et al., 2017).

### *Homologous recombination deficiency analysis for tissues*

To estimate genomic scar, we developed the 3DMed-HRD algorithm based on over 10,000 single-nucleotide polymorphisms (SNP) distributed across the human genome. Those SNPs were also included in 139-gene NGS assay. HRD was evaluated by the sum of the loss of heterozygosity (LOH), telomeric allelic imbalance (TAI), and large-scale state transition (LST).

### *Antibody Optimization for high-plexed immunofluorescence*

Prior to experiments, antibody staining specificity and sensitivity were assessed using a multi-organ array that contained 9 cancer tissue types (Outdo Biotech, Shanghai). Slides were cleared and processed for antigen retrieval, and all antibodies were used at the manufacturer's recommended concentrations with a 1-hour room temperature (RT) incubation. Staining patterns were evaluated by experienced pathologists and compared with patterns reported in literature and/or the Human Protein Atlas (<http://www.proteinatlas.org/>). The strongest staining and most specific antibodies were further tested to ensure that the antigen was not lost by the dye inactivation process during the cyclic process. This was accomplished by comparing staining on samples that were untreated or treated 1 or 6 times with the dye quenching process mimicking cyclic steps. Fifteen markers were included in the validation process: Pan-CK, Ki-67, CD3, CD4, CD8, FoxP3, CD20, CD68, CD11b, CD14, CD33, CD163, PD-1, PD-L1 and SMA. After the screening, optimal antibodies were chosen and non-labeled antibodies against underwent conjugation with either Cy3 or Cy5 bis-NHS-ester dyes according to manufacturer's protocols (Thermo Fisher A20186/A20187). All antibodies used in downstream high-plexed immunofluorescence are listed in Table S1.

### High-plexed cyclic fluorescence imaging

The high-plexed imaging of each slide was performed using sequential multiplexing of 2–4 markers along with DAPI counterstain. The cell DIVE-based imaging process employed a patented stain-bleach cycling method (Gerdes et al., 2013). The supporting information provides a detailed cycling workflow based on our experimental setup (Table S1). As above, FFPE slides were dewaxed, rehydrated and stained with iterative cycles of antibodies. After each staining and imaging round (20X magnification), fluorescence was quenched and slides were re-imaged to obtain residual background for autofluorescence correction. All samples were stained and imaged using the same antibody batch and DAPI at a time.

### Multiplexed image processing, spatial single cell data acquisition and processing

Upon collection of automated fluorescence image (AFI) files, data were processed using HALO software (Indica Labs). All images were registered and stacked based on DAPI alignment (Woolfe et al., 2011). For each channel, pathologically evaluation derived algorithm was used for foreground/background adjustment and selection. Those mainly considered mean intensity, maximum intensity, cell doublets and locational expression distribution (membrane, cytoplasm, and nucleus). Resultant spatial single cell quantitative expression profiles (ROI level) in every Field of View (FOV) were generated (Pan-CK, Ki-67, CD3, CD4, CD8, FoxP3, CD20, CD68, CD11b, CD14, CD33, CD163, PD-1, PD-L1 and SMA). Quality control measures were also implemented to ensure usable cell-level intensities, and manual scoring of tissue quality and segmentation was performed for every sample. The continuous expression matrix was used to construct t-SNE plots and maker-based pair-wise expression correlation plots.

### DSP whole transcriptome profiling of PDAC-HRD samples

The DSP experiment workflow was detailed previously (Merritt et al., 2020). Briefly, paired FFPE sections (5  $\mu$ m thickness) were deparaffinized with CitriSolv (DECON), rehydrated and subjected to antigen retrieval in 1x Tris-EDTA/pH 9 at 100 °C for 15 min in depressurized condition. For RNA target exposure, proteinase K (Thermo Scientific) digestion was performed at 1 ng/ml concentration for 15 min at 37 °C. Samples were then fixed in neutral-buffered formalin and hybridized with target-specific photocleavable barcoded DNA probes (WTA with 18,269 genes, nanoString) in a hybridization chamber overnight at 37 °C. Extra probes were washed away and co-stained with morphology markers: SYTO13 (Thermo Fisher Scientific, cat. no. 57575), panCK (Novus Biologicals, NBP2-33200, AF532, 1:400), CD45 (Cell Signaling Technology, 13917, AF594, 1:100), and  $\alpha$ -SMA (Abcam, ab267537, AF647, 1:200) for 1 hour at RT prior to loading onto the GeoMx DSP (nanoString). n=12 ROIs were collected per patient tissue and probes were constructed into sequencing libraries and QC checked prior to sequencing on a NovaSeq 6000 sequencing platform with a PE150 kit (illumina).

### DSP data preprocessing and analysis

FASTQ files for all ROIs were processed as previously described (Merritt et al., 2020). In brief, files were demultiplexed based on unique molecular identifiers (UMIs), mapped back with spatial barcode sequences and aggregated into a single count file using the GeoMx NGS pipeline and GeoMx Tool R package. The limit of quantitation (LOQ) was estimated by calculating the geometric mean of the negative control probes plus two geometric standard deviations of the negative control probes. Targets over the limit of quantitation in less than 1 % of ROIs were removed, and the filtered dataset was normalized using upper quartile (Q3) normalization (Hwang et al., 2022). Since our normalized

data was robust and rigorous to perfectly depict biological difference between ROI groups (adjacent, tumor, immune-stroma and fibroblast) without added inter-patient effects (Fig. 3B), we used these data for downstream analysis.

### Cell lines and mice

The human pancreatic cancer cell lines (PANC-1 and BxPC-3), the mice PAN02 pancreatic cancer cell lines and human THP-1 monocytes were purchased from ATCC. Cells were cultured in DMEM (Invitrogen, Carlsbad, CA, USA) or RPMI-1640 medium (Invitrogen, Carlsbad, CA, USA) supplemented with 10 % fetal bovine serum (FBS, Gibco, Carlsbad, CA, USA) and 1 % penicillin/streptomycin (Invitrogen) and cultured at 37°C in humidified air with 5 % CO<sub>2</sub>. Regular testing for mycoplasma contamination was conducted on all cell lines.

All animal studies were approved by the Institutional Animal Care and Use Committee of Southern Medical University. The C57BL/6 mice were adaptively housed in facilities for 7 days, subjected to daily observation. The PAN02 cells ( $1 \times 10^6$  cells/150  $\mu$ L per mouse) were subcutaneously injected into the right axilla. Tumor growth was monitored by measuring the tumors along the perpendicular long and short axes (length and width, respectively). Tumor volumes were calculated using the formula for the volume of a modified ellipsoid (volume =  $1/2 \times \text{length} \times \text{width}^2$ ). Upon reaching an average tumor volume of approximately 200 mm<sup>3</sup> in tumor-bearing mice, the mice were randomly divided into control group, Olaparib (PARPi) single-drug group, Aletuzumab (anti-CD52) single-drug group, PARPi combined with anti-CD52 group. Mice were euthanized after 3 weeks of drug treatment (three times a week), and the transplanted tumor mass was collected for flow cytometry assay. Drug preparation and dosages were as follows: the dosage of PARPi and anti-CD52 were prepared according to the ratio provided by Selleck.

### Cell co-culture assay and flow cytometry

THP-1 cells were re-suspended in 1640 medium and seeded into 6-well plates. Phorbol 12-myristate 13-acetate (PMA) was added to the medium. After 48 hours of induction of THP-1 cells, differentiated macrophages adhered to the wall were observed. After scraping and re-suspending the cells, cell counting was performed, and macrophages were seeded at a density of 150,000 cells per well in a 12-well plate. PANC-1 cells were incubated with PKH67. After incubation, PANC-1 cells were washed with PBS once, and each group of cells was trypsinized for cell counting. PANC-1 cells were then seeded at a density of 150,000 cells per well into the macrophage culture medium, with three replicate wells per group.

The cells were washed with PBS containing the fluorochrome-coupled antibodies against the indicated antigens. The cells were incubated at 4 °C in the dark, and washed twice with PBS and resuspended in fresh PBS for flow cytometry. Flow cytometry data were collected using BD FACSDiva Software 8.0.1, and subsequently analyzed with FlowJo software 10.8.1.

### Western blotting

Western blotting was performed following a previously described standard protocol, using anti-N-Cadherin (Cell Signaling Technology, 13116), anti- $\alpha$ -SMA (Abcam, ab5694), anti-Snail (Cell Signaling Technology, 3879), anti-Twist (Abcam, ab50887), anti-E-Cadherin (Cell Signaling Technology, 3195), anti-TGF-beta 1 (Abcam, ab314095), anti-phospho-T $\beta$ R1 (Invitrogen, PA5-40298), anti-T $\beta$ R1 (Invitrogen, PA5-98192), anti-Phospho-Smad2 (MCE, HY-P80853), anti-Smad2 (MCE, HY-P80324), anti-Phospho-Smad3 (MCE, HY-P80854), anti-Smad3 (MCE, HY-P80325) and anti- $\beta$ -actin (Servicebio, GB15001).

### Cell lineage assignment and quantification using multi-plexed fluorescence imaging data

For selected region-of-interests (ROIs), we pre-defined three levels of cell classification based on selected marker combinations (Table S2). Each level of classification was independent. We began to assign cells into major lineages based on one or two canonical markers for each cell lineage: T cells (CD3<sup>+</sup>), B cells (CD20<sup>+</sup>), macrophage (CD68<sup>+</sup>), myeloid cells (CD11b<sup>+</sup>/CD33<sup>+</sup>), monocytes (CD14<sup>+</sup>/CD11b<sup>+</sup>), fibroblasts (SMA<sup>+</sup>) and tumor cells (PanCK<sup>+</sup>) for classification 1, besides those also included cells with multiple positive markers or totally negative stain (only nuclei staining). We then used other known canonical markers to annotate sub-lineages within each cell class (classification 2). Lastly, we added PD-1 or PD-L1 checkpoints to annotate some cell subtypes of interests (classification 3). All three classifications were mutually exclusive. To avoid the inter-slide experimental bias, we normalized our data per ROI and obtained each cell subtype ratio based on total cell counts within individual ROI and these data were merged for inter-ROI and inter-sample data comparison.

### Cellular fraction-based analysis

To analyze inter-HRD group alterations, all ROIs were assigned into different HRD groups for downstream analysis. Cell-cell pairwise correlation was performed across all cell type ratio at ROI level. Significant association or avoidance patterns between cell types were defined as having a p-value of less than 0.05. For analysis of expression or program scores, a linear hybrid effect model was used to control for multiple sampling in the slide. Satterthwaite's approximate degree of freedom was employed to calculate the p value. The related coefficients were calculated using Spearman ratings.

### PDAC cellular neighborhood (CN) identification

To generate spatial cellular neighborhoods, we defined a "capture window" being the number (N) of nearest cells to a given cell, as previously described (Schurch et al., 2020). Each window was represented as a frequency vector containing the types of cells closest to a given cell (as indicated). We used classification 2 for CN analysis since PD-1/PD-L1 were not prevalent in our data (classification 3). We obtained all windows for each cell and generated collection of a vector (length of N) consisting of all cell types around a given cell. The resulting neighborhoods were clustered using Scikit-learn, a Python machine-learning library, and the MiniBatchKMeans clustering algorithm version 0.24.2 with default batch size = 100 and random\_state = 0 (Karimi et al., 2023). We performed subsequent CN analysis using the MiniBatchKMeans clustering algorithm version 1.1.2 with default batch size = 1024 and random\_state = 0. Every cell was subsequently allocated into a CN based on their defining window. To normalize the prevalence of each neighborhood across samples, we ensured that the neighborhood prevalence (frequency) for each sample was summed to 100%. CN frequencies were compared between HRD-nil and non-zero PDAC groups for CN identification.

### Spatial deconvolution and spatial mapping using DSP data

We used a default deconvolution method for DSP (SpatialDecon, R package) to infer a series of cell types within each ROI (Danaher et al., 2022). We used a default cell-to-gene matrix (safeTME) as well as a PDAC single-cell RNA-seq (GSE155698) derived matrix to deduce cell types for inter-HRD group comparison. We also employed other published computational tools compatible with DSP data to generate multiple cell fractions in all ROIs across HRD groups. Methods used included MCP-counter, consensusTME, EPIC, QuantIseq and xCell (Sturm et al., 2019). To evaluate cross-region cell type alteration dynamics, cell2location-WTA (a robust spatial cell distribution inferring method

optimized using DSP-WTA data) was used (Li et al., 2022b; Roberts et al., 2021). For this, public sc-RNAseq data for PDAC (GSE155698) was used and each HRD groups were analyzed separately across tumor, immune-stroma and fibroblast regions.

### Pathway enrichment analysis and spatial transcription programs identification using WGCNA

To leverage between the background noise and potential genes of interest, we first filtered genes based on p-values (FDR<0.05) and used those spatial differentially expressed gene sets. To derive core spatial transcriptional programs, we used unbiased expression network analysis method WGCNA (weighted gene co-expression network analysis) to identify transcription programs associated with different HRD phenotypes within tumor and fibroblast regions. For unbiased discovery, we used all genes (18,269) as input in WTA profiling and used the default scale-free topology fitting index (R<sup>2</sup>=0.85) and mean connectivity to obtain the best soft threshold. Transcriptional programs were identified under the dynamic cut with a minimal gene number set to 30 for each module. Most significant transcription programs (genes in each module) associated with HRD phenotypes at spatial levels were used in downstream spatial correlation analysis.

### DSP ROI-based spatial correlation and receptor-ligand correlation analysis

To investigate the interplay between the transcription programs embedded in epithelial/ fibroblast regions and various cell types within the immune-stroma, genes associated with WGCNA-derived modules relating to the HRD phenotypes were extracted and corresponding WTA gene expression profiles were used to compute the single sample GSEA score (ssGSEA score). The ssGSEA scores were plotted against individual cell abundance (derived from SpatialDecon) per individual ROIs for each group (Hwang et al., 2022). The correlation plot was then constructed and hierarchically clustered based on their Pearson correlation R<sup>2</sup> (-1-1) (Hwang et al., 2022). For ligand-receptor interaction analysis, known pairs were obtained from CellPhoneDB v2.0 (Efremova et al., 2020). To quantify potential ligand-receptor co-expression, all ROIs were assigned into three groups according to their spatial classes (PanCK, CD45 or SMA) and were compared inter- and intra-groups. The Spearman rank correlation was used to assess ROI-wise ligand-receptor expression for all paired segments representing non-self (juxtacrine) and self (autocrine) occurrences. To determine the ligand-receptor pair correlation between HRD groups, receptor-ligand co-expression correlations were calculated for each HRD groups and plotted group-wise. All statistical analyses were two-sided and used a significance level of P value ≤ 0.05. When appropriate, adjustments for multiple testing were made using the false discovery rate (FDR) (Korthauer et al., 2019). To calculate pathway scores for each ROI, the geometric means of normalized expression for each gene were used:

$$\text{Pathway score} = N \sqrt{\text{gene1.gene2.gene3.....geneN}}$$

### PDAC single-cell RNA-seq data acquisition and cell annotation

The datasets GSE155698 was processed using Seurat v4. Cells with a gene expression range of 300–10,000 genes and 500–100,000 UMIs were screened based on the mitochondrial gene fraction of less than 10%. After filtering, both datasets were re-normalized using Seurat's SCTransform, and the top 3000 highly variable genes (HVG) were selected and used to stabilize UMI count variance. The principal component analysis (PCA) was performed using highly variable genes (HVGs), and the shared nearest neighbor (SNN) graph and unified manifold approximation and projection (UMAP) were constructed by using Louvain algorithm and the first 30 principal components and clustering units. The major cell types were identified based on cross-

cohort typical cell type-labeled scores: Epithelial were labeled with EPCAM, KRT18, SOX4, MDK; acinar cells were labeled with REG1A, CTRB2, PRSS1; pericytes were labeled with RGS5, PDGFRB; B cells were labeled with CD79A, CD19, and MS4A1; CD4, CD3D, CD3E, and TRAC were used to identify CD4<sup>+</sup> T cells; and CD8A, CD8B, and GZMK were used to identify CD8<sup>+</sup> T cells; Natural killer cells (NKs) were labeled with KLRD1, GNLY and NKG7; regulatory T cells were labeled with FOXP3, IL2RA, TNFRSF4; dendritic cells were labeled with TOP2A, HLA-DMB, CD1C, and LAMP3; macrophages were labeled with CD68, FCGR1A, and ITGAX; mast cells were labeled with KIT, MS4A2, and RGS13; endothelial cells were labeled with CLDN5, CDH5, and RAMP2; and fibroblasts were labeled with C1R, COL1A2, and DCN; Granulocytes were labeled with CD300E, EREG, and S100A12. Finally, referring the cluster package (Zappia et al., 2018) and previous study (Wang et al., 2021b), fibroblasts were annotated as fibroblast-like cells, myofibroblasts, smooth muscle cells, and apCAFs. The resulting cell-gene matrix was used for DSP data deconvolution.

#### Developing R-based method for PDAC TME

To construct a cell deconvolution method at refined sub-histological level for PDAC, we started by extracting genes in DSP-WTA corresponding to 15 markers used in high-plexed immunofluorescence. We backwardly selected most relevant genes under the gene-gene correlation cutoff ( $R^2=0.4$ ) across ROIs for each cell type (annotated according to classification 2 in high-plex immunofluorescence) which then resulted in a minimal cell-gene input matrix for cell type deconvolution to function. The deconvoluted cell fractions were then plotted against the cellular fraction calculated by high-plex immunofluorescence and Spearman correlation was used to assess the prediction accuracy. To increase the predictive power, we performed this TME-based deconvolution comparison for three independent ROI groups (tumor, immunostroma and fibroblast-enriched) respectively. This process was iterated with step-wise increasing gene number until a correlation  $R^2$  to fall under 0.4 (with a sum of 2604 genes). The WTA deconvoluted dataset was ranked and optimal gene sets for three independent TME regions were selected and collapsed into a R package for TME cell type deconvolution (PDAC-Decon: <https://github.com/HongWF413/PDAC-Decon>).

#### Statistical analysis and workflow

All image analysis steps were performed in Python (version 3.7.12). Statistical analyses were conducted using R software (version 4.2.0). t-SNE and UMAP were used for dimensionality reduction analysis. Wilcoxon test was used to compare differences between two groups, while Kruskal-Wallis's test was used to compare differences among multiple groups. Data were presented as mean  $\pm$  S.E.M or mean  $\pm$  standard deviation. All statistical tests were indicated in the legends. Spearman analysis was used for correlation analysis. Unless otherwise indicated,  $P<0.05$  was considered to indicate statistically significant differences.

#### Software

All software is freely or commercially available and is listed in the Methods description.

#### CRediT authorship contribution statement

**Shisuo Du:** Writing – review & editing, Supervision, Methodology. **Min Yu:** Writing – review & editing, Supervision, Project administration, Investigation, Funding acquisition, Data curation, Conceptualization. **Xuexin Li:** Writing – review & editing, Software, Methodology. **Feng Zhang:** Validation, Software, Resources, Methodology, Investigation, Data curation. **Weifeng Hong:** Writing – review & editing, Writing – original draft, Visualization, Validation, Software, Project

administration, Formal analysis, Data curation. **JunMing Bi:** Validation, Resources, Methodology, Data curation. **Nan Wang:** Visualization, Software, Formal analysis, Data curation. **Dingwen Zhang:** Software, Resources, Methodology, Investigation. **ZhenTao Song:** Software, Resources, Methodology, Investigation. **Lusheng Wei:** Software, Project administration, Methodology, Data curation. **Minmin Chen:** Software, Methodology. **Gordon B Mills:** Writing – review & editing.

#### Declaration of interests

N.W is a full-time employee of Cosmos Wisdom Biotech and worked for Fynn Biotechnologies. Z.T.S is a full-time employee of Fynn Biotechnologies. G.B.M. is one of the SAB (Scientific Advisory Board) members or consults with AstraZeneca, Chrysallis Biotechnology, GSK, ImmunoMET, Ionis, Lilly, PDX Pharmaceuticals, Signalchem Life-sciences, Symphogen, Tarveda, Turbine, Zentalis Pharmaceuticals. G.B.M has stock options with Catena Pharmaceuticals, ImmunoMet, SignalChem, Tarveda. Other authors declare no competing interests.

#### Data Availability

Publicly available single cell transcriptome data from NSCLC was derived from GEO (accession number GEO: GSE155698). Additional information related to the data in this study is available from the lead contact upon request.

#### Acknowledgments

The research was supported by National Natural Science Foundation of China (Grant No. 82072741); High-level Hospital Construction Project of Guangdong Provincial People's Hospital (Grant No. DFJH2019015); the National Key Clinical Specialty Discipline Construction Program of China (Grant No. 2022YW030009); Shenzhen Bay Laboratory Open Fund (Grant No. KH012021016). We thank the team from Fynn Biotechnologies Ltd., for experimental supports and guidance on high-plexed immunofluorescence and DSP.

#### Appendix A. Supporting information

Supplementary data associated with this article can be found in the online version at [doi:10.1016/j.drug.2024.101115](https://doi.org/10.1016/j.drug.2024.101115).

#### References

- Aguirre, A.J., et al., 2018. Real-time genomic characterization of advanced pancreatic cancer to enable precision medicine. *Cancer Discov.* 8, 1096–1111. <https://doi.org/10.1158/2159-8290.CD-18-0275>.
- Bandala-Sanchez, E., et al., 2013. T cell regulation mediated by interaction of soluble CD52 with the inhibitory receptor Siglec-10. *Nat. Immunol.* 14, 741–748. <https://doi.org/10.1038/ni.2610>.
- Bandala-Sanchez, E., et al., 2018. CD52 glycan binds the proinflammatory B box of HMGB1 to engage the Siglec-10 receptor and suppress human T cell function. *Proc. Natl. Acad. Sci. USA* 115, 7783–7788. <https://doi.org/10.1073/pnas.1722056115>.
- Bianchi, A., et al., 2023. Cell-autonomous Cxcl1 sustains tolerogenic circuitries and stromal inflammation via neutrophil-derived TNF in pancreatic cancer. *Cancer Discov.* <https://doi.org/10.1158/2159-8290.CD-22-1046>.
- Biffi, G., et al., 2019. IL1-Induced JAK/STAT Signaling Is Antagonized by TGFbeta to Shape CAF Heterogeneity in Pancreatic Ductal Adenocarcinoma. *Cancer Discov.* 9, 282–301. <https://doi.org/10.1158/2159-8290.CD-18-0710>.
- Cancer Genome Atlas Research Network, 2017. Electronic address, a. a. d. h. e. & Cancer Genome Atlas Research, N. Integrated Genomic Characterization of Pancreatic Ductal Adenocarcinoma. *e113 Cancer Cell* 32, 185–203. <https://doi.org/10.1016/j.ccell.2017.07.007>.
- Capula, M., et al., 2022. Role of drug catabolism, modulation of oncogenic signaling and tumor microenvironment in microbe-mediated pancreatic cancer chemoresistance. *Drug Resist. Update.: Rev. Comment. Antimicrob. Anticancer Chemother.* 64, 100864 <https://doi.org/10.1016/j.drug.2022.100864>.
- Carstens, J.L., et al., 2017. Spatial computation of intratumoral T cells correlates with survival of patients with pancreatic cancer. *Nat. Commun.* 8, 15095 <https://doi.org/10.1038/ncomms15095>.

- Casolino, R., et al., 2021. Homologous Recombination Deficiency in Pancreatic Cancer: A Systematic Review and Prevalence Meta-Analysis. *J. Clin. Oncol.* 39, 2617–2631. <https://doi.org/10.1200/JCO.20.03238>.
- Chabanon, R.M., et al., 2021. Targeting the DNA damage response in immuno-oncology: developments and opportunities. *Nat. Rev. Cancer* 21, 701–717. <https://doi.org/10.1038/s41568-021-00386-6>.
- Chavez-Galan, L., Ollerros, M.L., Vesin, D., Garcia, I., 2015. Much More than M1 and M2 Macrophages, There are also CD169(+) and TCR(+) Macrophages. *Front Immunol.* 6, 263. <https://doi.org/10.3389/fimmu.2015.00263>.
- Chen, Y., et al., 2023a. Association between homologous recombination deficiency and outcomes with platinum and platinum-free chemotherapy in patients with triple-negative breast cancer. *Cancer Biol. Med* 20, 155–168. <https://doi.org/10.20892/j.issn.2095-3941.2022.0525>.
- Chen, X., et al., 2022. Mutant p53 in cancer: from molecular mechanism to therapeutic modulation. *Cell Death Dis.* 13, 974. <https://doi.org/10.1038/s41419-022-05408-1>.
- Chen, S., et al., 2023b. Macrophages in immunoregulation and therapeutics. *Signal Transduct. Target. Ther.* 8, 207. <https://doi.org/10.1038/s41392-023-01452-1>.
- Cooks, T., et al., 2018. Mutant p53 cancers reprogram macrophages to tumor supporting macrophages via exosomal miR-1246. *Nat. Commun.* 9, 771. <https://doi.org/10.1038/s41467-018-03224-w>.
- Danaher, P., et al., 2022. Advances in mixed cell deconvolution enable quantification of cell types in spatial transcriptomic data. *Nat. Commun.* 13, 385. <https://doi.org/10.1038/s41467-022-28020-5>.
- Deczkowska, A., Weiner, A., Amit, I., 2020. The Physiology, Pathology, and Potential Therapeutic Applications of the TREM2 Signaling Pathway. *Cell* 181, 1207–1217. <https://doi.org/10.1016/j.cell.2020.05.003>.
- Efremova, M., Vento-Tormo, M., Teichmann, S.A., Vento-Tormo, R., 2020. CellPhoneDB: inferring cell-cell communication from combined expression of multi-subunit ligand-receptor complexes. *Nat. Protoc.* 15, 1484–1506. <https://doi.org/10.1038/s41596-020-0292-x>.
- Elyada, E., et al., 2019. Cross-Species Single-Cell Analysis of Pancreatic Ductal Adenocarcinoma Reveals Antigen-Presenting Cancer-Associated Fibroblasts. *Cancer Discov.* 9, 1102–1123. <https://doi.org/10.1158/2159-8290.CD-19-0094>.
- Fraunce, C., et al., 2020. MMR Deficiency is Homogeneous in Pancreatic Carcinoma and Associated with High Density of Cd8-Positive Lymphocytes. *Ann. Surg. Oncol.* 27, 3997–4006. <https://doi.org/10.1245/s10434-020-08209-y>.
- Freed-Pastor, W.A., et al., 2021. The CD155/TIGIT axis promotes and maintains immune evasion in neoantigen-expressing pancreatic cancer. *e1314 Cancer Cell* 39, 1342–1360. <https://doi.org/10.1016/j.ccell.2021.07.007>.
- García-Alonso, L., et al., 2021. Mapping the temporal and spatial dynamics of the human endometrium in vivo and in vitro. *Nat. Genet.* 53, 1698–1711. <https://doi.org/10.1038/s41588-021-00972-2>.
- Gerdes, M.J., et al., 2013. Highly multiplexed single-cell analysis of formalin-fixed, paraffin-embedded cancer tissue. *Proc. Natl. Acad. Sci. USA* 110, 11982–11987. <https://doi.org/10.1073/pnas.1300136110>.
- Golan, T., et al., 2019. Maintenance Olaparib for Germline BRCA-Mutated Metastatic Pancreatic Cancer. *N. Engl. J. Med* 381, 317–327. <https://doi.org/10.1056/NEJMoa1903387>.
- Guantay, L., et al., 2023. Deoxycytidine kinase (dCK) inhibition is synthetic lethal with BRCA2 deficiency. *Drug Resist Updat* 67, 100932. <https://doi.org/10.1016/j.drup.2023.100932>.
- Halbrook, C.J., et al., 2022. Differential integrated stress response and asparagine production drive symbiosis and therapy resistance of pancreatic adenocarcinoma cells. *Nat. Cancer* 3, 1386–1403. <https://doi.org/10.1038/s43018-022-00463-1>.
- Hamarshah, S., Gross, O., Brummer, T., Zeiser, R., 2020. Immune modulatory effects of oncogenic KRAS in cancer. *Nat. Commun.* 11, 5439. <https://doi.org/10.1038/s41467-020-19288-6>.
- Hamerman, J.A., et al., 2006. Cutting edge: inhibition of TLR and FcR responses in macrophages by triggering receptor expressed on myeloid cells (TREM)-2 and DAP12. *J. Immunol.* 177, 2051–2055. <https://doi.org/10.4049/jimmunol.177.4.2051>.
- Han, S., et al., 2022. Single-cell profiling of microenvironment components by spatial localization in pancreatic ductal adenocarcinoma. *Theranostics* 12, 4980–4992. <https://doi.org/10.7150/thno.73222>.
- Han, J., DePinho, R.A., Maitra, A., 2021. Single-cell RNA sequencing in pancreatic cancer. *Nat. Rev. Gastroenterol. Hepatol.* 18, 451–452. <https://doi.org/10.1038/s41575-021-00471-z>.
- Hao, Y., et al., 2022. Combinatorial therapeutic approaches of photodynamic therapy and immune checkpoint blockade for colon cancer treatment. *Mol. Biomed.* 3, 26. <https://doi.org/10.1186/s43556-022-00086-z>.
- Herold, S., Mayer, K., Lohmeyer, J., 2011. Acute lung injury: how macrophages orchestrate resolution of inflammation and tissue repair. *Front Immunol.* 2, 65. <https://doi.org/10.3389/fimmu.2011.00065>.
- Heskeith, M., Sahin, K.B., West, Z.E., Murray, R.Z., 2017. Macrophage Phenotypes Regulate Scar Formation and Chronic Wound Healing. *Int J. Mol. Sci.* 18 <https://doi.org/10.3390/ijms18071545>.
- Hong, W., et al., 2024. Deciphering the immune modulation through deep transcriptomic profiling and therapeutic implications of DNA damage repair pattern in hepatocellular carcinoma. *Cancer Lett.* 582, 216594 <https://doi.org/10.1016/j.canlet.2023.216594>.
- Huang, J., et al., 2021. Worldwide Burden of, Risk Factors for, and Trends in Pancreatic Cancer. *Gastroenterology* 160, 744–754. <https://doi.org/10.1053/j.gastro.2020.10.007>.
- Hu, B., et al., 2022. Subpopulations of cancer-associated fibroblasts link the prognosis and metabolic features of pancreatic ductal adenocarcinoma. *Ann. Transl. Med.* 10, 262.
- Hwang, W.L., et al., 2022. Single-nucleus and spatial transcriptome profiling of pancreatic cancer identifies multicellular dynamics associated with neoadjuvant treatment. *Nat. Genet.* 54, 1178–1191. <https://doi.org/10.1038/s41588-022-01134-8>.
- Ino, Y., et al., 2013. Immune cell infiltration as an indicator of the immune microenvironment of pancreatic cancer. *Br. J. Cancer* 108, 914–923. <https://doi.org/10.1038/bjc.2013.32>.
- Jhunjhunwala, S., Hammer, C., Delamarre, L., 2021. Antigen presentation in cancer: insights into tumour immunogenicity and immune evasion. *Nat. Rev. Cancer* 21, 298–312. <https://doi.org/10.1038/s41568-021-00339-z>.
- Jia, Q., Chu, H., Jin, Z., Long, H., Zhu, B., 2022. High-throughput single-cell sequencing in cancer research. *Signal Transduct. Target. Ther.* 7, 145. <https://doi.org/10.1038/s41392-022-00990-4>.
- Kadera, B.E., et al., 2014. Locally advanced pancreatic cancer: association between prolonged preoperative treatment and lymph-node negativity and overall survival. *JAMA Surg.* 149, 145–153. <https://doi.org/10.1001/jamasurg.2013.2690>.
- Karimi, E., et al., 2023. Single-cell spatial immune landscapes of primary and metastatic brain tumours. *Nature* 614, 555–563. <https://doi.org/10.1038/s41586-022-05680-3>.
- Karolchik, D., et al., 2004. The UCSC Table Browser data retrieval tool. *Nucleic Acids Res* 32, D493–D496. <https://doi.org/10.1093/nar/gkh103>.
- Korthauer, K., et al., 2019. A practical guide to methods controlling false discoveries in computational biology. *Genome Biol.* 20, 118. <https://doi.org/10.1186/s13059-019-1716-1>.
- Krzyszczak, P., Schloss, R., Palmer, A., Berthiaume, F., 2018. The Role of Macrophages in Acute and Chronic Wound Healing and Interventions to Promote Pro-wound Healing Phenotypes. *Front Physiol.* 9, 419. <https://doi.org/10.3389/fphys.2018.00419>.
- Kung, H.-C., Yu, J., 2023. Targeted therapy for pancreatic ductal adenocarcinoma: Mechanisms and clinical study. *MedComm* 4, e216. <https://doi.org/10.1002/mco2.216>.
- Lai, E., et al., 2021. BRCA-mutant pancreatic ductal adenocarcinoma. *Br. J. Cancer* 125, 1321–1332. <https://doi.org/10.1038/s41416-021-01469-9>.
- Liang, X., et al., 2018. PD-L1 in pancreatic ductal adenocarcinoma: a retrospective analysis of 373 Chinese patients using an in vitro diagnostic assay. *Diagn. Pathol.* 13, 5. <https://doi.org/10.1186/s13000-017-0678-4>.
- Lin, Q., et al., 2024. Fibroblast growth factor receptor 1 inhibition suppresses pancreatic cancer chemoresistance and chemotherapy-driven aggressiveness. *Drug Resist Updat* 73, 101064. <https://doi.org/10.1016/j.drup.2024.101064>.
- Li, X., et al., 2017. Targeting of tumour-infiltrating macrophages via CCL2/CCR2 signalling as a therapeutic strategy against hepatocellular carcinoma. *Gut* 66, 157–167. <https://doi.org/10.1136/gutjnl-2015-310514>.
- Li, W., et al., 2022a. Identification and prognostic analysis of biomarkers to predict the progression of pancreatic cancer patients. *Mol. Med* 28, 43. <https://doi.org/10.1186/s10020-022-00467-8>.
- Liu, H., et al., 2018. Nuclear cGAS suppresses DNA repair and promotes tumorigenesis. *Nature* 563, 131–136. <https://doi.org/10.1038/s41586-018-0629-6>.
- Li, B., et al., 2022b. Benchmarking spatial and single-cell transcriptomics integration methods for transcript distribution prediction and cell type deconvolution. *Nat. Methods* 19, 662–670. <https://doi.org/10.1038/s41592-022-01480-9>.
- Liu, W., et al., 2021. Siglec-15 promotes the migration of liver cancer cells by repressing lysosomal degradation of CD44. *FEBS Lett.* 595, 2290–2302. <https://doi.org/10.1002/1873-3468.14169>.
- Liu, Y. e, et al., 2023. Emerging phagocytosis checkpoints in cancer immunotherapy. *Signal Transduct. Target. Ther.* 8, 104. <https://doi.org/10.1038/s41392-023-01365-z>.
- Li, H., Durbin, R., 2009. Fast and accurate short read alignment with Burrows-Wheeler transform. *Bioinformatics* 25, 1754–1760. <https://doi.org/10.1093/bioinformatics/btp324>.
- Mantovani, A., Allavena, P., Marchesi, F., Garlanda, C., 2022. Macrophages as tools and targets in cancer therapy. *Nat. Rev. Drug Discov.* 21, 799–820. <https://doi.org/10.1038/s41573-022-00520-5>.
- Marabelle, A., et al., 2020. Efficacy of Pembrolizumab in Patients With Noncolorectal High Microsatellite Instability/Mismatch Repair-Deficient Cancer: Results From the Phase II KEYNOTE-158 Study. *J. Clin. Oncol.* 38, 1–10. <https://doi.org/10.1200/JCO.19.02105>.
- Merritt, C.R., et al., 2020. Multiplex digital spatial profiling of proteins and RNA in fixed tissue. *Nat. Biotechnol.* 38, 586–599. <https://doi.org/10.1038/s41587-020-0472-9>.
- Molgora, M., et al., 2020. TREM2 Modulation Remodels the Tumor Myeloid Landscape Enhancing Anti-PD-1 Immunotherapy. *e817 Cell* 182, 886–900. <https://doi.org/10.1016/j.cell.2020.07.013>.
- Mouw, K.W., Goldberg, M.S., Konstantinou, P.A., D'Andrea, A.D., 2017. DNA Damage and Repair Biomarkers of Immunotherapy Response. *Cancer Discov.* 7, 675–693. <https://doi.org/10.1158/2159-8290.CD-17-0226>.
- Movahedi, K., et al., 2010. Different tumor microenvironments contain functionally distinct subsets of macrophages derived from Ly6C(high) monocytes. *Cancer Res* 70, 5728–5739. <https://doi.org/10.1158/0008-5472.CAN-09-4672>.
- Nguyen, L., J. W.M.M., Van Hoek, A., Cuppen, E., 2020. Pan-cancer landscape of homologous recombination deficiency. *Nat. Commun.* 11, 5584. <https://doi.org/10.1038/s41467-020-19406-4>.
- Nomi, T., et al., 2007. Clinical significance and therapeutic potential of the programmed death-1 ligand/programmed death-1 pathway in human pancreatic cancer. *Clin. Cancer Res* 13, 2151–2157. <https://doi.org/10.1158/1078-0432.CCR-06-2746>.
- Ogle, M.E., Segar, C.E., Sridhar, S., Botchwey, E.A., 2016. Monocytes and macrophages in tissue repair: Implications for immunoregenerative biomaterial design. *Exp. Biol. Med* (Maywood) 241, 1084–1097. <https://doi.org/10.1177/1535370216650293>.

- Ozdemir, B.C., et al., 2014. Depletion of carcinoma-associated fibroblasts and fibrosis induces immunosuppression and accelerates pancreas cancer with reduced survival. *Cancer Cell* 25, 719–734. <https://doi.org/10.1016/j.ccr.2014.04.005>.
- Qin, Q., Yu, R., Eriksson, J.E., Tsai, H.I., Zhu, H., 2024. Cancer-associated fibroblasts in pancreatic ductal adenocarcinoma therapy: Challenges and opportunities. *Cancer Lett.* 591, 216859 <https://doi.org/10.1016/j.canlet.2024.216859>.
- Qiu, H., et al., 2021. TREM2: Keeping Pace With Immune Checkpoint Inhibitors in Cancer Immunotherapy. *Front Immunol.* 12, 716710 <https://doi.org/10.3389/fimmu.2021.716710>.
- Reschke, R., Gajewski, T.F., 2022. CXCL9 and CXCL10 bring the heat to tumors. *Sci. Immunol.* 7, eabq6509 <https://doi.org/10.1126/sciimmunol.abq6509>.
- Roberts, K. et al. Transcriptome-wide spatial RNA profiling maps the cellular architecture of the developing human neocortex. *bioRxiv*, 2021.2003.2020.436265, (doi:10.1101/2021.03.20.436265) (2021).
- Samstein, R.M., et al., 2021. Mutations in BRCA1 and BRCA2 differentially affect the tumor microenvironment and response to checkpoint blockade immunotherapy. *Nat. Cancer* 1, 1188–1203. <https://doi.org/10.1038/s43018-020-00139-8>.
- Schalck, A., et al., 2022. Single-Cell Sequencing Reveals Trajectory of Tumor-Infiltrating Lymphocyte States in Pancreatic Cancer. *Cancer Discov.* 12, 2330–2349. <https://doi.org/10.1158/2159-8290.CD-21-1248>.
- Schurch, C.M., et al., 2020. Coordinated Cellular Neighborhoods Orchestrate Antitumoral Immunity at the Colorectal Cancer Invasive Front. *e1319 Cell* 182, 1341–1359. <https://doi.org/10.1016/j.cell.2020.07.005>.
- Siegel, R.L., Miller, K.D., Wagle, N.S., Jemal, A., 2023. Cancer statistics, 2023. *CA Cancer J. Clin.* 73, 17–48. <https://doi.org/10.3322/caac.21763>.
- Smith, B.A.H., Bertozzi, C.R., 2021. The clinical impact of glycobiology: targeting selectins, Siglecs and mammalian glycans. *Nat. Rev. Drug Discov.* 20, 217–243. <https://doi.org/10.1038/s41573-020-00093-1>.
- Springfeld, C., et al., 2019. Chemotherapy for pancreatic cancer. *Presse Med* 48, e159–e174. <https://doi.org/10.1016/j.lpm.2019.02.025>.
- Sturm, G., et al., 2019. Comprehensive evaluation of transcriptome-based cell-type quantification methods for immuno-oncology. *Bioinformatics* 35, i436–i445. <https://doi.org/10.1093/bioinformatics/btz363>.
- Su, D., et al., 2017. High performance of targeted next generation sequencing on variance detection in clinical tumor specimens in comparison with current conventional methods. *J. Exp. Clin. Cancer Res* 36, 121. <https://doi.org/10.1186/s13046-017-0591-4>.
- Ubertini, V., et al., 2015. Mutant p53 gains new function in promoting inflammatory signals by repression of the secreted interleukin-1 receptor antagonist. *Oncogene* 34, 2493–2504. <https://doi.org/10.1038/onc.2014.191>.
- de Visser, K.E., Joyce, J.A., 2023. The evolving tumor microenvironment: From cancer initiation to metastatic outgrowth. *Cancer Cell* 41, 374–403. <https://doi.org/10.1016/j.ccell.2023.02.016>.
- Wang, N., Li, X., Wang, R., Ding, Z., 2021a. Spatial transcriptomics and proteomics technologies for deconvoluting the tumor microenvironment. *Biotechnol. J.* 16, e2100041 <https://doi.org/10.1002/biot.202100041>.
- Wang, J., et al., 2019. Siglec-15 as an immune suppressor and potential target for normalization cancer immunotherapy. *Nat. Med* 25, 656–666. <https://doi.org/10.1038/s41591-019-0374-x>.
- Wang, Z., et al., 2021b. Deciphering cell lineage specification of human lung adenocarcinoma with single-cell RNA sequencing. *Nat. Commun.* 12, 6500. <https://doi.org/10.1038/s41467-021-26770-2>.
- Werba, G., et al., 2023. Single-cell RNA sequencing reveals the effects of chemotherapy on human pancreatic adenocarcinoma and its tumor microenvironment. *Nat. Commun.* 14, 797. <https://doi.org/10.1038/s41467-023-36296-4>.
- Woolfe, F., Gerdes, M., Bello, M., Tao, X., Can, A., 2011. Autofluorescence removal by non-negative matrix factorization. *IEEE Trans. Image Process* 20, 1085–1093. <https://doi.org/10.1109/TIP.2010.2079810>.
- Xiong, D., Wang, Y., You, M., 2020. A gene expression signature of TREM2(hi) macrophages and gammadelta T cells predicts immunotherapy response. *Nat. Commun.* 11, 5084. <https://doi.org/10.1038/s41467-020-18546-x>.
- Zappia, L., Phipson, B., Oshlack, A., 2018. Exploring the single-cell RNA-seq analysis landscape with the scRNA-tools database. *PLoS Comput. Biol.* 14, e1006245 <https://doi.org/10.1371/journal.pcbi.1006245>.
- Zhang, M., et al., 2021a. Pancreatic cancer cells render tumor-associated macrophages metabolically reprogrammed by a GARP and DNA methylation-mediated mechanism. *Signal Transduct. Target. Ther.* 6, 366. <https://doi.org/10.1038/s41392-021-00769-z>.
- Zhang, S.M., et al., 2021b. M2-polarized macrophages mediate wound healing by regulating connective tissue growth factor via AKT, ERK1/2, and STAT3 signaling pathways. *Mol. Biol. Rep.* 48, 6443–6456. <https://doi.org/10.1007/s11033-021-06646-w>.
- Zhao, J., et al., 2024. Riboflavin protects against pancreatic cancer metastasis by targeting TGF-beta receptor 1. *Bioorg. Chem.* 146, 107274 <https://doi.org/10.1016/j.bioorg.2024.107274>.
- Zhu, S., et al., 2022. Homologous recombination deficiency (HRD) score in aggressive prostatic adenocarcinoma with or without intraductal carcinoma of the prostate (IDC-P). *BMC Med* 20, 237. <https://doi.org/10.1186/s12916-022-02430-0>.